THE UNIVERSITY OF CHICAGO

A MEASUREMENT OF THE COSMIC MICROWAVE BACKGROUND GRAVITATIONAL LENSING POTENTIAL AND ITS POWER SPECTRUM FROM 500 DEG^2 OF SPTPOL DATA

A DISSERTATION SUBMITTED TO
THE FACULTY OF THE DIVISION OF THE PHYSICAL SCIENCES
IN CANDIDACY FOR THE DEGREE OF
DOCTOR OF PHILOSOPHY

DEPARTMENT OF ASTRONOMY AND ASTROPHYSICS

BY
LAURA MONICA MOCANU

CHICAGO, ILLINOIS
AUGUST 2017

This thesis is dedicated to the universe.

Your assumptions are your windows on the world.

Scrub them off every once in a while,

or the light won't come in.

Isaac Asimov

TABLE OF CONTENTS

LIST OF FIGURES

LIST OF TABLES

ACKNOWLEDGMENTS

I want to thank my advisor, John Carlstrom, for his support, and for giving me the opportunity to be part of this outstanding collaboration. I feel very lucky to have worked with such a bright, inspiring and committed group. I want to thank Tom Crawford for the enormous help he provided on all of the projects that I worked on and throughout graduate school. I want to thank my fellow graduate students on the project, Kyle Story, whom I've learned a lot from, Tyler Natoli, for always asking great questions, and Lindsey Bleem, for being a good mentor. Thanks to Abby Crites and Stephen Hoover for helping me get started with data analysis of the SPTpol data, and to Zhen Hou for his aid with simulations and running on computing clusters. I want to thank Jason Gallicchio and Jason Henning for their help with my analysis questions. Thanks to Brad Benson, who has provided me with great feedback on my projects and during group meetings. Thanks to Amy Bender for her guidance down at Pole. I wish to thank my classmates, Hsin-Yu Chen, Ke Fang, Sean Johnson, and Vinicius Miranda, for going through all those homework sets and our first year together and for being supportive friends ever since. I am grateful for everyone's help along the way.

ABSTRACT

Weak gravitational lensing by large-scale structure in the universe causes deflections in the paths of cosmic microwave background (CMB) photons. This effect introduces statistical anisotropy in the observed CMB temperature and polarization fields. The signature of lensing can be used to reconstruct the projected gravitational lensing potential with a quadratic estimator technique; this provides a measure of the integrated mass distribution out to the surface of last scattering, sourced primarily from redshifts between 0.1 and 5. The power spectrum of the lensing potential encodes information about the geometry of the universe and the growth of structure and can be used to place constraints on the sum of neutrino masses and dark energy. High signal-to-noise mass maps from CMB lensing are also powerful for cross-correlating with other tracers of large-scale structure and for delensing the CMB in search for primordial gravitational waves. This thesis describes a high signal-to-noise reconstruction of the CMB gravitational lensing potential and a measurement of its power spectrum using data from 500 deg^2 of sky observed between 2012 and 2015 with the polarization-sensitive receiver SPTpol, installed on the South Pole Telescope (SPT). We find the ratio of the lensing spectrum to a theoretical ΛCDM model to be $A_{\mathrm{MV}} = 0.94 \pm 0.05\,(\mathrm{stat.}) \pm 0.04\,(\mathrm{sys.})$. This measurement represents a 17.1σ constraint on the lensing amplitude and a 41σ detection of lensing effects.

CHAPTER 1

INTRODUCTION

Measurements of the cosmic microwave background (CMB) have contributed to enormous recent progress in cosmology. Gravitational interaction with structures in the universe modifies the statistics of the observed CMB in a way that allows for the reconstruction of the integrated gravitational potential that causes the deflections. In this thesis, we describe a measurement of the CMB lensing potential using data from the South Pole Telescope. We begin with a brief review of basic cosmology, the CMB and the ΛCDM model, and introduce the concept of gravitational lensing in context of the CMB.

1.1 Cosmology

Cosmology has progressed greatly over the past century and especially during the last two decades. The discovery of the expansion of the universe [10] has led to the Big Bang paradigm, a model in which the universe started out in a state of extreme density and temperature, and has been expanding and cooling since.

Inflation, a period of exponential expansion of the early universe [11] proposed in the 1980s, is the current favored theory for explaining the origin of primordial density fluctuations. It is a period of superluminal expansion postulated to occur 10^{-35} s after the Big Bang, and it causes the universe to expand by over 60 e-foldings. Causally connected points are brought out of causal contact, and any existing curvature is reduced by large factors.

Simple models of inflation assume that a scalar field ϕ, called the inflaton, exists throughout space. During inflation, the inflaton slowly rolls down and causes the exponential expansion. Quantum mechanical fluctuations in the inflaton potential seed density perturbations that are expanded to macroscopic scales. Inflation leaves behind Gaussian scalar perturbations with a nearly scale-invariant spectrum. These perturbations will grow into the cosmic

structures we observe today. The inflaton ultimately decays and the energy in its potential is converted into particles during a period called reheating. The particles dominate the energy density of the universe until dark energy dominates once more.

The universe is comprised of four main elements. The radiation component consists of photons and neutrinos, at early times when they are still relativistic. Baryons are the matter that makes up visible stars, galaxies and dust, and comprise ∼5% of the energy density of the universe. Dark matter is a form of matter that does not emit light and is inferred through its gravitational effects, making up ∼26% of the energy. Dark energy is the dominant part of the energy density budget today, at ∼69%, is presumed to exist throughout space, and is responsible for the current accelerated expansion of the universe.

The universe can be approximated as homogeneous and isotropic on large scales, and its expansion as a function of time is parametrized by the scale factor $a(t)$, which is unity today and is related to the redshift parameter z as $a = \frac{1}{1+z}$. The Hubble parameter H parametrizes the rate of expansion: $H(a) = \frac{1}{a}\frac{da}{dt}$. The rate of expansion and acceleration of the universe can be described through the Friedmann equations:

$$H^2 = \left(\frac{\dot{a}}{a}\right)^2 = \frac{8\pi G}{3c^2}\rho(a) - \frac{\kappa}{a^2c^2} \tag{1.1}$$

$$\frac{\ddot{a}}{a} = -\frac{4\pi G}{3c^2}\rho(1+3\omega), \tag{1.2}$$

where G is the gravitational constant, ρ is the energy density of the universe, κ parametrizes the curvature of the universe, with $\kappa \in [-1, 1]$, $\omega = \frac{p}{\rho}$ is the equation of state parameter of the fluid, and the derivatives are with respect to time. Taking into account the rate of expansion, the current age of the universe is ∼13.8 Gyrs. Each component's energy density scales differently with the scale factor, contributing to the total energy density of the universe as:

$$\Omega(a) = \Omega_\gamma a^{-4} + \Omega_m a^{-3} + \Omega_k a^{-2} + \Omega_\Lambda, \tag{1.3}$$

where Ω_i is the energy density of component i, γ stands for radiation (which includes neutrinos in this definition), m stands for matter as the sum of baryons and cold dark matter, k stands for curvature, and Λ for dark energy in models which assume a cosmological constant or vacuum energy is responsible for the accelerated expansion. The energy density of the universe is first dominated by radiation, then matter, and finally dark energy until today.

1.2 The Cosmic Microwave Background

At early times, the universe is filled with a photon-baryon plasma; radiation and baryons are tightly coupled, and the universe is opaque to electromagnetic radiation. Baryons and photons fall into dark matter potential wells, but the photons provide radiation pressure, pushing the fluid out of overdense regions. The interaction of the two opposing forces gives rise to acoustic oscillations.

As the universe expands, this plasma cools until photons do not have the energy required to ionize hydrogen anymore. This happens when the universe is roughly 380,000 years old. Protons and electrons bind into neutral hydrogen atoms, and the universe becomes transparent to light. This marks the so-called "epoch of recombination". Photons are not coupled to baryons anymore and begin free-streaming through the universe, giving rise to the cosmic microwave background (CMB) that we see today. The CMB is a relic of this early epoch [12]. We observe the surface of last scattering produced during this era in a shell centered on our location. This offers a snapshot of the universe as it was at this very early time, when photons traced the density fluctuations in the plasma. This is, essentially, the earliest picture of the universe that we can directly image.

The observed CMB is nearly isotropic and a nearly perfect blackbody with T=2.73 K, with anisotropies at the 10 μK level, or one part in 10^5 [13]. The angular power spectrum of the anisotropies exhibits a pattern of peaks and troughs imprinted by the acoustic oscillations in the primordial photon-baryon plasma. The characteristic size of the hot and cold spots is

about one degree. The harmonics are increasingly suppressed towards smaller scales. This is caused by photon diffusion out of overdense regions and the feature is called the "damping tail" of the CMB.

The near-isotropy of the CMB across superhorizon scales, that could not apparently have been in causal contact in the past, was one of the "problems" in cosmological theory that inflation was introduced as a solution to, along with the flatness of the universe and the absence of magnetic monopoles.

The "thickness" of the surface of last scattering is very small compared to the distance to it, meaning that recombination is a rapid process. However, it happens slow enough to give rise to local quadrupoles in the photon intensity. The presence of these local quadrupoles of the radiation field cause the CMB to become polarized at the $\sim$10% level through Thomson scattering by the photons off of electrons [14]. The scattered radiation is linearly polarized.

As they travel through the universe from the surface of last scattering, CMB photons experience other occasional interactions that generate secondary anisotropies in the observed CMB. Among those processes are the Sunyaev-Zel'dovich thermal and kinematic (tSZ and kSZ) effects, the integrated Sachs-Wolfe (ISW) effect, and gravitational lensing. The tSZ effect is the inverse Compton scattering of CMB photons by energetic electrons in galaxy clusters, where the photons gain energy. The kSZ effect occurs when the electrons have a bulk flow velocity and the photons are Doppler shifted to higher or lower frequency, based on the orientation of the velocity. The ISW effect is the gravitational redshifting of photons due to evolving potential wells along the line of sight, between us and the surface of last scattering. Finally, gravitational lensing is the bending of the photon paths due to the gravitational interaction with matter along the path. We focus on analyzing the lensing effect in this thesis.

The CMB was predicted to exist in the 1940s [15]. It was discovered serendipitously in 1964 by radio astronomers Penzias and Wilson [16], who were later awarded the Nobel Prize

in 1978 for their discovery. CMB measurements have been steadily improving over the past two decades. The CMB anisotropies were first measured with the COBE satellite [13], which also made the first precise measurement of the CMB blackbody spectrum [17]. The following satellite missions, *WMAP* [18] and *Planck* [1], mapped the anisotropies with better angular resolution and lower noise. Their measurements cover the whole sky, pinning down the large scales. Ground-based experiments like the South Pole Telescope, ACT, BICEP/Keck and POLARBEAR have made yet deeper and sharper measurements over smaller patches of sky.

The CMB is a very powerful tool for constraining cosmological models. Temperature anisotropy measurements are now at the cosmic variance limit on scales down to a few arcminutes [19, 20, 21, 22]. Figure 1.1 shows recent TT power spectrum measurements. While these can still be improved on smaller scales with deeper maps and larger area surveys, the current focus is on mapping the polarization anisotropies. Significant progress has been made on this front in the past few years [8, 23, 24, 1], and rapid development continues. Polarization adds complementary information and is significantly less contaminated by astrophysical foregrounds down to smaller angular scales.

Throughout this analysis, we use multipole numbers ℓ when working with data in Fourier space. The multipole number ℓ is related to angular size of a feature on the sky by $\ell \sim \frac{180^\circ}{\theta}$.

The Stokes parameters are a set of four parameters that can be used to describe the polarization state of radiation. The parameters are labeled as I, Q, U, and V. I describes total intensity, Q and U describe the degree of linear polarization along the chosen x axis and at a 45° angle to that, respectively, and V describes the circular polarization (and is null in our case).

The CMB polarization field can be decomposed into even-parity E-modes (curl-free) and odd-parity B-modes (divergence-free) [25, 26]. E and B are related to Q and U for a multipole

ℓ by:

$$E_\ell = \quad Q_\ell \cos 2\phi_\ell + U_\ell \sin 2\phi_\ell \tag{1.4}$$

$$B_\ell = \quad -Q_\ell \sin 2\phi_\ell + U_\ell \cos 2\phi_\ell \tag{1.5}$$

where $\phi_\ell = \arctan \ell_y/\ell_x$ is the phase angle between ℓ_x and ℓ_y.

To first order, scalar density perturbations generate only E-mode polarization. Gravitational waves generate both E- and B-modes. Inflation gives rise to primordial gravitational waves, which produce a small B-mode polarization signal in the CMB, which is brightest at multipoles below 100 (see Figure 1.3). The strength of the signal is parametrized by the tensor-to-scalar ratio r. Detecting this signal is the foremost goal of CMB efforts as a direct probe of early universe physics. A measurement of r would reveal the energy scale of inflation and constrain classes of inflation models, advancing our understanding of fundamental physics and potentially of quantum gravity.

1.3 The ΛCDM model

The "Lambda Cold Dark Matter" (ΛCDM) model has emerged as a good description for most cosmological measurements to date. The model assumes a flat universe dominated by dark energy with an equation of state parameter $w = -1$, in accelerated expansion. It describes the universe using six parameters: the baryon density today $\Omega_b h^2$, the cold dark matter density today $\Omega_c h^2$, the angular size of the sound horizon at last scattering θ_s, the optical depth to reionization τ, the amplitude of primordial scalar fluctuations Δ^2_R, and the power-law index of the scalar spectrum n_s. All other parameters can be derived from these six.

The standard ΛCDM model has so far been very successful at explaining the observations, and its six parameters have been measured with increasing precision. Still, there is ample

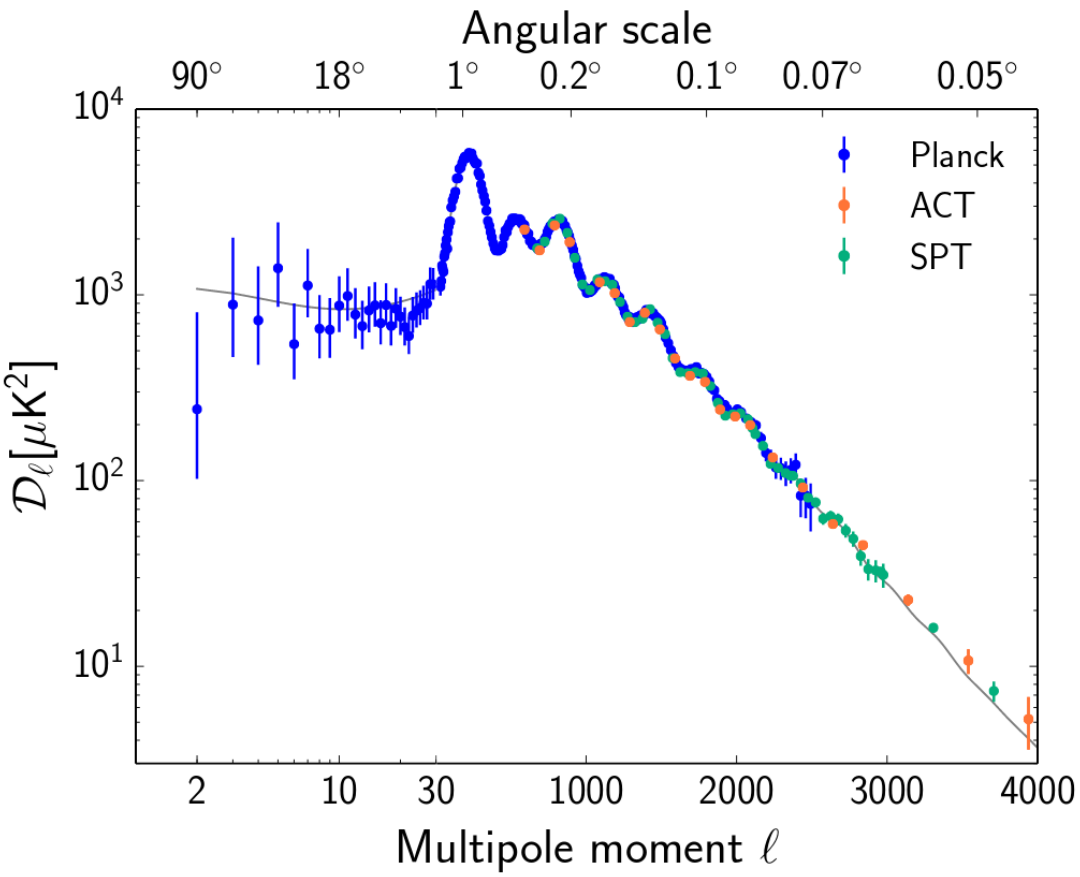

Figure 1.1: Summary of recent CMB temperature power spectrum measurements, taken from Planck XI (2015) [1].

room for improvement, and extensions to this model are yet poorly constrained by current data. Polarization measurements are now adding new information and the potential to break parameter degeneracies.

1.4 Gravitational Lensing of the CMB

CMB photons get deflected by large scale structures in the universe as they travel from the surface of last scattering to us. This process is called gravitational lensing. A comprehensive review of CMB lensing can be found in Lewis and Challinor [4]

The magnitude of the deflection angles introduced by lensing is on the order of $2'$, but

the deflections are coherent over 2° scales. This is because the structures that cause the deflections have degree-size angular scales on the sky.

Lensing has several main effects on the CMB fields. First, lensing smooths the temperature and E-mode power spectra [27]. Although the deflection angles are small, the fact that they are correlated over scales comparable to that of the primary CMB acoustic peaks means that lensing has significant effect over these scales as well. Lensing hot or cold spots can result in the magnification or demagnification of these features; they will not be enlarged or shrunk on average, but their size distribution will become wider, which corresponds to a broadening of the acoustic peaks at the percent-level. Another way to think about this is that local magnification shifts the local CMB power spectrum to the left (towards smaller multipoles or larger scales), while demagnification shifts it to the right, resulting in this peak widening effect. Figure 1.2 shows how the temperature CMB spectrum changes with lensing. Lensing dominates the CMB temperature power spectrum on arcminute scales ($\ell \sim 3000$) due to the transfer of power from large to small scales. Essentially, large-scale lenses smooth the peaks, while small-scale lenses lens the large-scale temperature gradient and introduce power on small scales, in the damping tail [28]. The E-mode spectrum changes by a fractionally larger amount since the unlensed EE peaks are sharper.

In case of the unlensed CMB, anisotropy modes with different wave vectors are uncorrelated. The second effect of lensing is that it correlates CMB Fourier modes that were initially independent. In other words, it introduces statistical anisotropy in the covariance of the CMB, so that the covariance now depends on direction on the sky and the lensing structures present along the line of sight. Lensing introduces statistical anisotropy into the CMB when considering a fixed lensing potential, or non-Gaussianity when marginalized over realizations of the lensing potential [28].

Third, lensing converts some primordial E-modes into B-modes [29], which are a contaminant for a potential primordial gravitational wave signal. There are no primordial B-modes

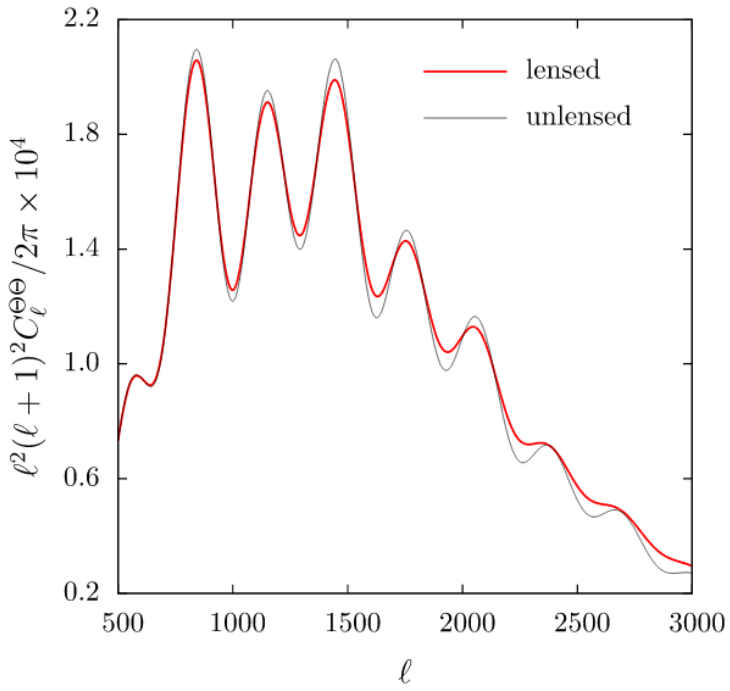

Figure 1.2: Angular power spectrum of lensed (red) and unlensed (grey) CMB temperature anisotropies for a fiducial cosmology, taken from [2].

on small scales, so all of the measured B-modes at high multipole numbers ($\ell \gtrsim 1000$) are due to lensing (or foregrounds). Figure 1.3 shows the theoretical power spectrum of the lensing B-modes. The lensed B-modes have a nearly flat C_ℓ spectrum for multipoles below 1000, resembling an instrumental white noise level of 5 μK-arcmin.

Lensing does not change the frequency of the photons, so the lensed CMB has the same blackbody frequency dependence as the unlensed CMB. Lensing also conserves surface brightness, or the number of photons observed per unit solid angle. For these two reasons, lensing of a completely isotropic CMB would be impossible to detect.

Figure 1.4 shows the power spectrum of the deflection angle. The deflection power peaks around a multipole of $\ell \sim 50$, which corresponds to a coherence length of a few degrees.

In this work, we treat lensing of the CMB as "weak lensing". The arcminute deflection angles are small enough that the weak lensing regime holds for CMB lensing. This means

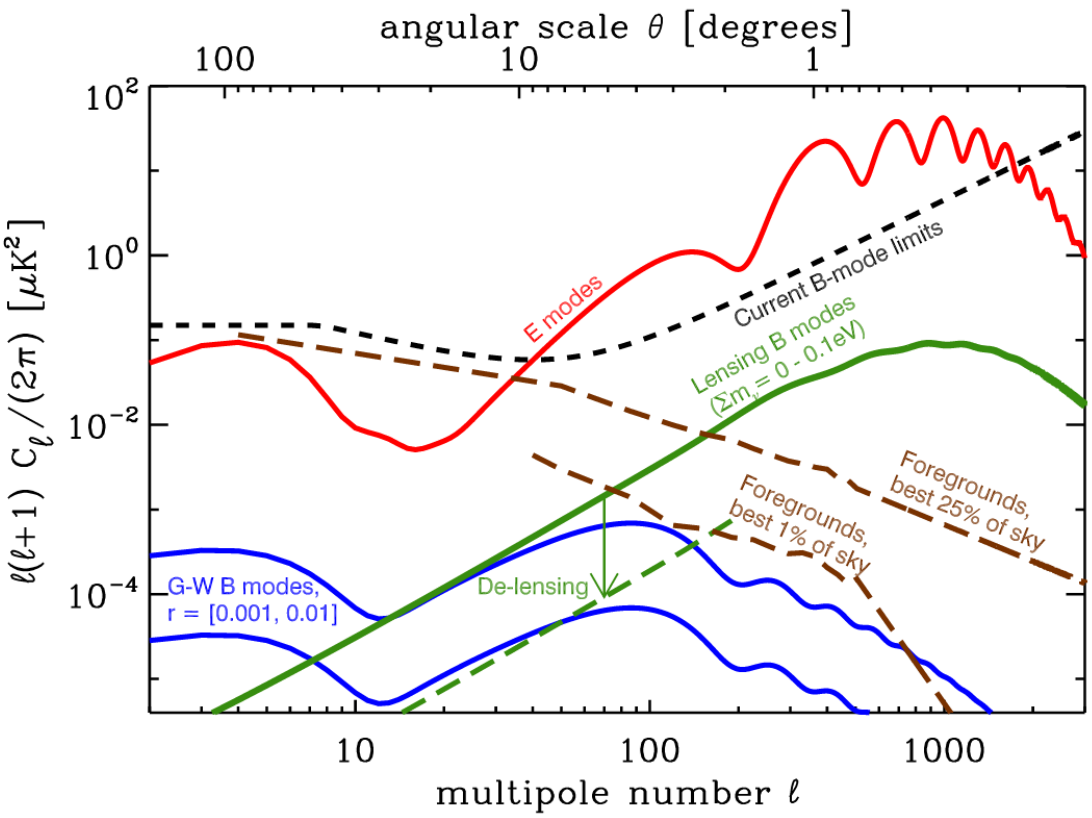

Figure 1.3: Power spectrum of CMB E-modes (red), lensing B-modes (green) and gravitational-wave B-mode signal for tensor-to-scalar ratios of $r = 0.001$ and $r = 0.01$ (blue), taken from [3].

that the Born approximation is valid: the effects of lensing can be calculated using the potential gradients along the undeflected photon path.

The CMB is very smooth on arcminute scales due to diffusion damping, such that the dominant lensing effect is by large scale structures close to the linear regime. Thus, the lensing is not in the "strong" regime in the sense of producing intersecting lines of sight, multiple images and caustics.

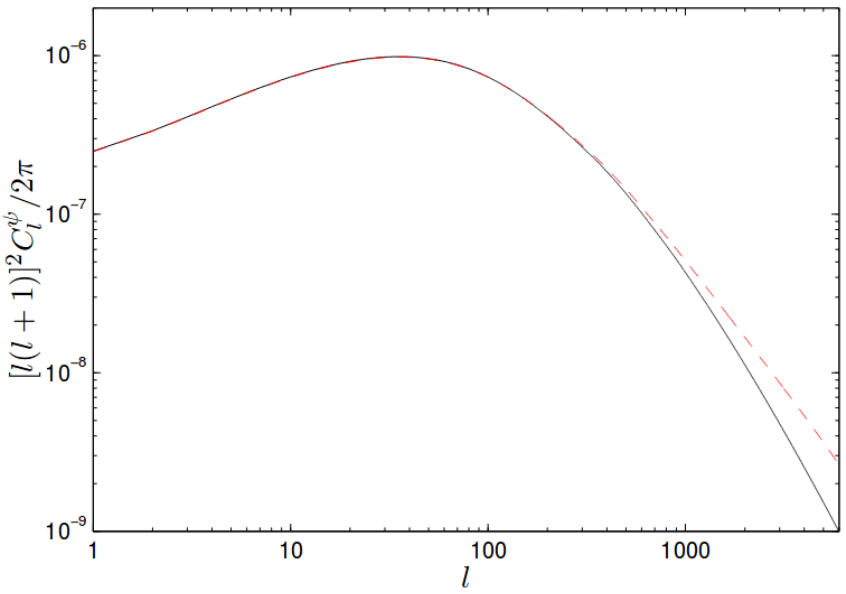

Figure 1.4: The power spectrum of the CMB deflection angle for a ΛCDM model, calculated with CAMB, taken from Lewis and Challinor [4]. The solid line shows the linear theory spectrum and the dashed line includes non-linear corrections from HALOFIT.

1.4.1 Motivation

There are a number of reasons the CMB is a good lensing source. It is the most distant light that can be observed; it is sourced at the surface of last scattering, at a known redshift $z \sim 1100$, and it covers the whole sky. Its statistics are well-known, and the unlensed CMB can be treated as a statistically isotropic Gaussian random field, completely characterized by its power spectrum. This means that every mode is drawn from a complex Gaussian with zero mean and variance that depends only on the length of the wavevector and not its direction.

CMB lensing also probes all the mass integrated out to the surface of last scattering. Lensing directly probes structure over a broad range in redshifts, roughly $0.1 < z < 5$, with a peak around $z \sim 2$. Figure 1.5 shows the cumulative contribution of different redshifts to the deflection power. CMB lensing thus probes matter at higher redshifts than, for instance, galaxy lensing. CMB lensing has the advantage that it probes the matter power spectrum

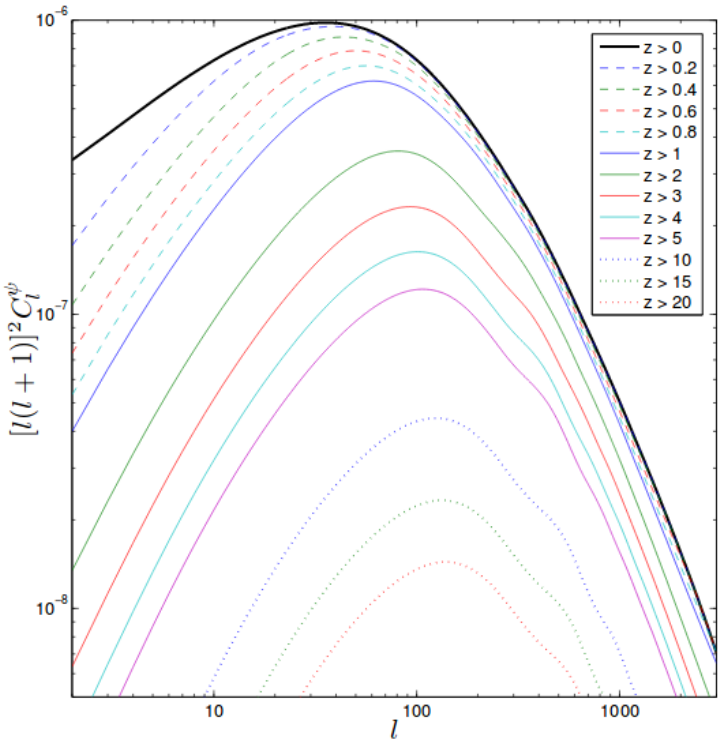

Figure 1.5: The cumulative contribution of different redshifts to the power spectrum of the lensing potential for a ΛCDM model, taken from Lewis and Challinor [4].

directly and not through a biased tracer, and suffers from little astrophysical uncertainty.

There is a strong motivation to study CMB lensing. Lensing encodes information about the growth of large scale structure and the geometry of the universe. It can be used to place constraints on cosmological parameters, notably the matter density Ω_m, the RMS linear matter fluctuation σ_8, and the sum of neutrino masses Σm_ν.

Observations of solar and atmospheric neutrino oscillations have measured a difference in mass between neutrino eigenstates and thus placed a lower bound on the sum of neutrino masses of $\Sigma m_\nu \gtrsim 58$ meV. Measurements of CMB lensing are a complementary way to constrain neutrino masses. Massive neutrinos damp growth of structure on scales smaller than the free-streaming length, so the matter power spectrum is suppressed on small scales, and that also translates into a suppression of the lensing power spectrum.

Lensing can also help constrain the curvature of the universe, the equation of state of dark energy, modified gravity, and the effective number of relativistic species.

Cross-correlating a CMB lensing map with other tracers of large scale-structure like galaxy density and weak lensing shear maps, such as those obtained with the Dark Energy Survey, yields information about the correlation between luminous matter and dark matter and can constrain galaxy bias, as well as enable tomographic studies [30].

Delensing can be used to improve constraints on primordial B-modes. Delensing consists in using a map of E-modes and a map of the lensing potential to produce an estimate of the lensed B-modes and subtract it from the measured B-modes to uncover the potential imprint of primordial gravitational waves.

1.4.2 Previous measurements

The first detection of CMB lensing was made by cross-correlating a *WMAP* lensing map with radio galaxy counts [31].

The effects of lensing have been measured in the CMB temperature power spectrum in data from ACT [20], SPT [32, 19], and Planck [33]. The full lensing reconstruction has been performed on temperature data in SPT-SZ [34, 6] (the latter of which combined SPT-SZ and *Planck* data), ACT [20], and *Planck* [35].

CMB lensing was measured in polarization data first in cross-correlation [36], by forming a B-mode template though lensing the SPTpol measured E-modes with a lensing potential estimated from Herschel cosmic infrared background (CIB) data, and crossing it with the measured SPTpol B-mode map. The lensing power spectrum was then measured from polarization data in POLARBEAR [8], SPTpol [37], *Planck* [5], ACTpol [7]. *Planck* [5] has placed a 2.5% constraint on the amplitude of the lensing potential; their reconstruction covers a large fraction of the sky, but only has signal-to-noise around unity for a few modes at $L \sim 50$. This work closely follows the analysis in [37], the first lensing reconstruction and

power spectrum from SPTpol, that used data from a 100 $\deg^2$ "deep field".

Cross-correlations between lensing and other tracers of structure, for example DES Science Verification data – galaxy density [30], galaxy shear [38, 39] – have been measured.

Delensing has only recently been performed on data. [40] delensed temperature *Planck* data, while [41] demonstrated delensing in polarization, also performed internally with *Planck* data by undoing the lensing deflections. Also, [42] delensed SPTpol data using a Herschel CIB estimate for the lensing potential.

1.5 Outline

This chapter has reviewed the basics of CMB phenomenology and of its gravitational lensing. We discuss the telescope and camera used for taking the data in Chapter 2. We describe the observations and data processing in Chapter 3. We detail the lensing analysis theory and pipeline in Chapter 4. In Chapter 5, we describe the creation and processing of the simulations used in the analysis. We present the main results of this analysis, the lensing map and power spectrum, in Chapter 6. In Chapter 7, we detail the uncertainty budget and present systematic tests. We conclude and discuss future prospects in Chapter 8.

CHAPTER 2

INSTRUMENT

2.1 The South Pole Telescope

The South Pole Telescope [43, 44] is a 10 meter diameter off-axis Gregorian telescope located at the Amundsen-Scott South Pole Station in Antarctica, built for dedicated CMB observations over a wide range of scales. It has arcminute resolution at 150 GHz and a square degree field of view. Figure 2.1 shows the telescope.

It is located at the South Pole because this is the best site on Earth for CMB observations. It's exceptionally dry, so there is little water vapor in the atmosphere to absorb millimeter radiation. It is at high altitude, 9300 ft or ∼2800 m (but the pressure altitude is closer to 11000 ft or 3300 m), so the radiation has less atmosphere to pass through, and the atmosphere is very stable since the sun rises and sets only once a year and there is no daily heating. The same patch of sky can be observed continuously for the whole year.

There have been three receivers installed on the SPT so far. The first receiver, SPT-SZ, was installed in 2007 and was sensitive only to intensity (temperature) fluctuations. Between 2008 and 2011, it was used to survey a 2500 $\deg^2$ field in three frequency bands centered at 95, 150 and 220 GHz [19]. The bands are inside windows of high atmospheric transmission.

The second camera, SPTpol, was a polarization-sensitive receiver installed on the SPT in 2012, which performed observations until the end of 2016 at two frequencies, 95 and 150 GHz. This analysis uses data from this camera, which is described in more detail in the next section.

The third generation camera, SPT-3G [45], has been deployed at Pole in early 2017. It has 2700 multichroic, three-frequency pixels with 2 polarizations, equivalent to 16200 total detectors. The secondary optics, receiver cryostat, readout electronics, and detectors have been redesigned with significant improvements and replaced. The camera will map the sky

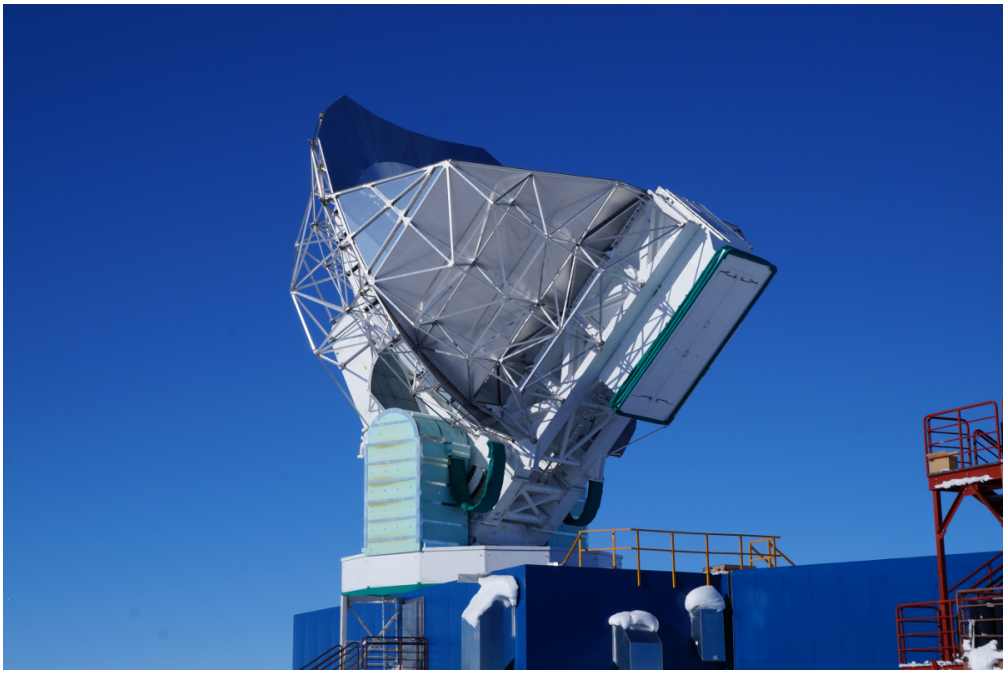

Figure 2.1: The South Pole Telescope.

20 times faster and map the survey area at twice lower noise than SPTpol.

2.2 SPTpol camera

The SPTpol receiver consists of 1536 polarization-sensitive transition edge sensor (TES) bolometer detectors. Of those, there are 1176 detectors, or 588 dual-polarization pixels, in seven central modules observing at 150 GHz [46], and 360 detectors in 180 pixels arranged around those modules observing at 95 GHz [47]. Figure 2.2 shows the focal plane.

The bolometers heat up when they absorb incoming radiation. The detectors are operated in the transition between normal resistance and superconducting (i.e. null) resistance, at ∼500 mK, such that a small change in temperature caused by absorbing radiation leads to a large change in resistance. The current from the detectors is amplified using superconducting quantum interference devices (SQUIDs) and read out using a digital frequency-domain multiplexing system (DfMux) [48, 49]. The SPTpol TES detectors are background-limited

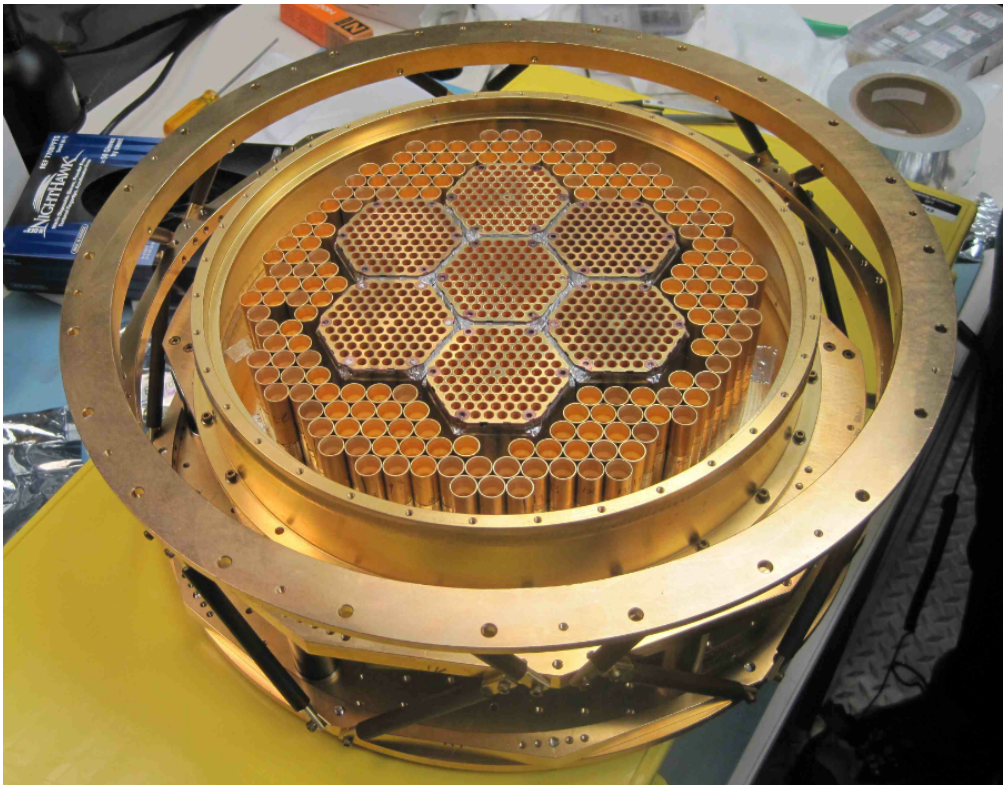

Figure 2.2: SPTpol focal plane. *Credit: B. Benson*

(limited by shot noise from the random arrival time of photons). This means that the only way to build a more sensitive instrument is to add more detectors.

2.3 Survey

Between April 2012 and April 2013, SPTpol was used to survey a 100 $\deg^2$ field called the "deep field". This area was chosen to maximize sensitivity to B-modes produced by gravitational lensing of E-modes. SPTpol was then used to observe a 500 $\deg^2$ field, the "survey field", until the end of 2016. This field has complete overlap, by design, with the BICEP/Keck survey, and is a low-foreground patch. The analysis of this "survey field" is the focus of this thesis.

Figure 2.3 shows the SPT survey fields, plotted on top of an IRAS dust map. SPT-SZ

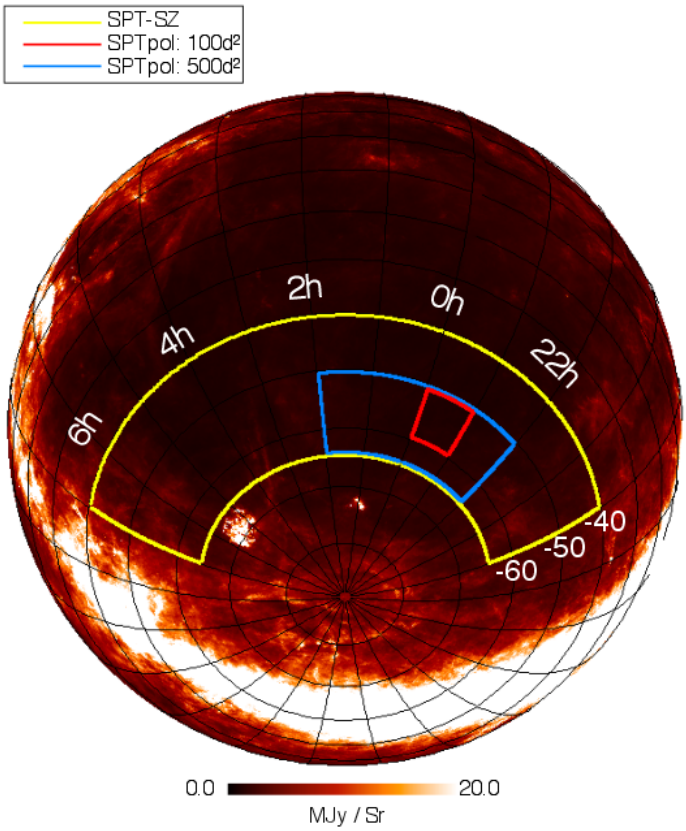

Figure 2.3: SPT survey fields plotted on top of an IRAS dust map. Yellow contour shows the 2500 deg^2 SPT-SZ survey region, intended to be surveyed again by SPT-3G. Red shows the 100 deg^2 "deep" SPTpol field, and blue shows the 500 deg^2 main SPTpol survey field used in this work.

surveyed the 2500 deg^2 yellow area. The survey extends from 20^h to 7^h in right ascension (R.A.) and from $-65°$ to $-40°$ in declination (dec.). The SPTpol "deep" and "survey" fields are shown inside this area. SPT-3G is expected to survey the full 2500 deg^2 field again.

SPT's arcminute resolution and low noise levels make it a great instrument for studying CMB lensing.

CHAPTER 3

OBSERVATIONS AND DATA PROCESSING

This chapter details how the data used in this analysis are acquired and processed. We describe the observing strategy, the filtering, data cuts, mapmaking and masking. The process is similar to that used in [23, 50, 37].

3.1 Observations

This analysis makes use of data of the 500 $\deg^2$ survey field, which extends from 22^h to 2^h in R.A. and from $-65°$ to $-50°$ in dec. The field was observed 3491 times over $\sim$9000 hours between April 30, 2013 and October 27, 2015. The field was observed for the 2016 season as well, but those data are not included in this analysis.

The SPT takes thousands of observations of the same field by scanning over it, as the detectors are sensitive to changes in millimeter-wave brightness. Each time, it observes the field by scanning back and forth in azimuth (at constant elevation), then stepping $9.2'$ in elevation, and repeating until the field is covered once. Every left or right pass of the telescope across the field is called a scan. The set of scans representing one complete mapping of the field is defined as an observation. Observations are repeated at 18 starting elevations (dither steps) that are 0.5' apart, in order to improve coverage.

The field was observed using two strategies. Beginning 2013, the field was observed using a "lead-trail" scanning strategy, where the field is divided into two halves in R.A. The telescope first observes the lead half as described above, and then switches to the trail half such that they are both observed over the same range in azimuth, and therefore the same patch of ground. This allows for the possibility to remove any ground contamination that might be found by differencing the two halves. It proved unnecessary to perform a lead-trail analysis since no contamination was observed, so the two halves are simply combined to

produce a full map of the field. The lead-trail observations are taken at a scan speed of 1.09 degrees per second in azimuth, equivalent to 0.59 deg/sec on the sky at the center of the field. In May 2014, the scanning strategy was switched to full-field, scanning along the full R.A. range of the field. The full-field scans are taken at 2 deg/sec in azimuth, or 1.1 deg/sec on the sky. Faster scanning allows for better separation between sky signals and low-frequency detector and noise. Angular frequency relates to temporal frequency by $f = \frac{lv_{\rm sky}}{360^\circ}$, where $v_{\rm sky}$ is the scan speed on the sky in deg/sec, ℓ is the multipole for the size of the feature, and f is the temporal frequency at which the feature will appear in the time-ordered data.

Pointing information is gathered by a two-step process. An online pointing model with an accuracy of a few arcminutes is used during observations. This is later corrected using an offline pointing model. The offline pointing correction is calculated based on a ten-parameter model that takes into consideration telescope boom flexure due to gravity, the tilt of the azimuth bearing axis, the tilt of the elevation axis, and corrections for telescope metrology, thermometry, and atmospheric refraction.

Aside from field observations, the telescope also takes calibration data. We take observations of RCW38 and MAT5A, two HII regions in the galaxy with known temperature, once per fridge cycle, which lasts 36 hours. These are used to calibrate detector timestreams. The MAT5A observations are also used for correcting the pointing. We also take fast, short RCW38 measurements in between observations, for calculating changes to the pointing.

Regular measurements of a calibrator, which is a chopped thermal source behind the secondary mirror, are taken to interpolate the calibration between RCW38 observations. Elevation nods, where the telescope moves in elevation, are used to measure the change in sensitivity as a function of elevation. The atmospheric loading changes as a function of elevation as the airmass that the telescope is observing through changes. Noise stares, where the telescope is not moving, are used to characterize the noise properties of each detector.

3.2 Timestream filtering

The raw data consists of time-ordered data (TOD), also called timestreams, which represent the electrical current required to keep the bolometer in its superconducting transition bias point, recorded as a function of time, for every bolometer.

We filter the timestreams to remove noisy data. Below we describe this filtering. The time-ordered data are recorded at 190.7 Hz. We downsample them by a factor of 2 to reduce computational needs.

We high-pass the data to remove low-frequency instrumental and atmospheric noise. For every scan, a Legendre polynomial is subtracted from each detector's timestream as an effective high-pass filter. We choose a 3^{rd} order polynomial for the lead-trail scans and a 5^{th} order polynomial for the full-field scans. We combine this with a high-pass filter at multipole ℓ=100. We also low-pass the TOD at a multipole ℓ=7500 to avoid higher frequency noise aliasing into the signal due to the map pixelization.

Regions within $5'$ of point sources brighter than 50 mJy at 150 GHz are masked in the timestreams during filtering to avoid ringing artifacts. Two spectral lines of the pulse tube cooler, together with their harmonics (up to the third) are removed, i.e. notch filtered in Fourier space.

Interactions within the digital frequency-domain multiplexing readout system cause cross-talk between detectors, especially those read out on the same resonance comb, at the 1% level. This manifests as small negative copies of the signal in neighboring detectors' timestreams. This cross-talk is corrected at the timestream level. A detector cross-talk matrix is constructed by comparing single-detector maps of RCW38 with templates of RCW38 averaged across the focal plane but offset and scaled to be detector-specific.

3.3 Cuts

We apply data quality cuts at three levels: scan data for one bolometer, single bolometer data for one observation, and whole observations.

At the scan level, data for a scan of a given bolometer is removed in case a "glitch" (sharp spike or DC jump) is present, generally caused by a cosmic ray or a change in SQUID bias point respectively. A scan TOD is also removed if the RMS noise for one detector is 5σ away from the median of all detectors. 8.9% of scans are removed for these reasons.

At the detector level, detectors with too high or too low noise in the 1-3 Hz signal band are removed from the whole observation. Detectors that exhibit low signal-to-noise during calibration observations are cut as well. Both partners in each dual-polarization pixel are cut if one of them is flagged. 864 out of the 1176 150 GHz detectors survive these cuts on average.

At the observation level, observations with high excess power at $\ell < 300$ in Q and U maps are removed. A statistic χ is defined as:

$$\chi = \log_{10}\left(\frac{\langle N_\ell^{XX}\rangle_{\ell<300}}{\mathrm{median}(N_\ell^{XX})}\right) \tag{3.1}$$

where $XX \in [QQ, UU]$ and N_ℓ^{XX} is the power spectrum of the noise in Q and U maps, obtained by differencing left-going and right-going data. Maps are removed for $\chi > 1$ for either Q or U. This removes maps with unusually large noise on large scales. 501 out of 4127 observations are cut in this manner. Observations with incomplete coverage of the field are cut as well.

3.4 Relative calibration

The timestreams are converted to sky power (units of μK_{CMB}) from bolometer gains that are obtained from RCW38 observations and calibrator stares.

A relative gain correction is applied between the two detectors in the same pixel by finding the relative gain factors such that the difference in power is minimal while keeping the total power is constant. The factors used are averages across an observation.

Polarization angles and efficiencies are calculated for each detector from observations of an external polarized calibrator.

3.5 Mapmaking

The timestreams are combined into maps using the pointing information, polarization angles, and weights for every detector [51, 52]. For every observation, timestream weights are calculated from the polarization efficiency $\eta_{\rm p}$ and the RMS noise amplitude n of a detector in the 1-3 Hz range. Both detectors in a pixel are assigned the same weight. The noise power is calculated by differencing left-going and right-going scans. Detector weights are calculated from polarization efficiency and noise RMS, $w \propto (\eta_{\rm p}/n)^2$.

The timestreams d_{ti} corresponding to detector i are binned into weighted Stokes T, Q and U map pixel α using the pointing information, weights w_i, and polarization angles θ_i:

$$\begin{aligned} T^W_{i\alpha} &= \sum_t A_{ti\alpha}\ w_i\ d_{ti} \\ Q^W_{i\alpha} &= \sum_t A_{ti\alpha}\ w_i\ d_{ti}\ \cos 2\theta_i \\ U^W_{i\alpha} &= \sum_t A_{ti\alpha}\ w_i\ d_{ti}\ \sin 2\theta_i, \end{aligned} \tag{3.2}$$

where $A_{ti\alpha}$ is the pointing matrix and t denotes the time sample. A 3x3 weight matrix W_α is constructed for each pixel by summing over all detectors. This includes information about the correlations between T, Q and U. One can then compute unweighted maps:

$$\{\hat{T}, \hat{Q}, \hat{U}\}_\alpha = W_\alpha^{-1}\{\hat{T}^W_\alpha, \hat{Q}^W_\alpha, \hat{U}^W_\alpha\}. \tag{3.3}$$

The maps have $1'$ resolution and are constructed using the Lambert azimuthal equal-area projection.

We present maps in units of $K_{\rm CMB}$, which signifies the change in temperature of a 2.73 K blackbody that would be required to produce the power fluctuation observed. The conversion factor between intensity and temperature is the derivative of the blackbody function dB_ν/dT evaluated at 2.73 K.

Throughout this analysis, we use the flat-sky approximation and equate multipole numbers ℓ with $2\pi|\mathbf{u}|$, where $\mathbf{u}$ is the Fourier conjugate of an angle on the sky small enough that the curvature of the patch and we can replace spherical harmonic transforms with two-dimensional Fourier transforms.

The Q and U maps are combined in Fourier space to produce E-mode and B-mode maps. E-mode maps are constructed by [53]:

$$E_{\boldsymbol{\ell}} = Q_{\boldsymbol{\ell}} \cos 2\phi_{\boldsymbol{\ell}} + U_{\boldsymbol{\ell}} \sin 2\phi_{\boldsymbol{\ell}}. \tag{3.4}$$

where $\phi_{\boldsymbol{\ell}} = \arctan \ell_y/\ell_x$. B-mode maps are made using the χ_B method described in [54]. In practice, this construction of E and B happens inside the C-inverse filter that we describe in the next chapter.

We coadd all of the observations into one coadded map that is used in the lensing analysis. By coadding many observations of the same field, the noise averages down and the signal to noise of the sky signal increases. The noise level in the coadded maps is 6.6 μK–arcmin in temperature and 9.4 μK–arcmin in polarization over the multipole range $1000 < \ell < 3000$. The map depth is similar to that of the 100 deg^2 deep field used in the [37] analysis, but the map covers five times the sky area.

Temperature, Q and U maps are shown in Figures 3.3, 3.4 and 3.5.

3.6 Beam

We need a measurement of the instrumental beam, or the response of the telescope to a point source, in order to properly perform the lensing analysis. We measure the beam from seven observations of Venus, specifically from averaging the cross-spectra between all pairs of those observations. To check the beam measurement on large scales, as well as to obtain an absolute calibration, we compute the cross-spectrum of 150 GHz SPTpol observations with the *Planck* 143 GHz temperature map over the same patch of sky, over the multipole range $600 < \ell < 1000$. The *Planck* data is mock-observed with the SPT scanning and filtering information in order to perform the comparison over the same sky modes, and the same apodization mask is used for both in order to remove mode-coupling effects. The beams are matched at $\ell = 800$. They agree so well that only the Venus beam is used in the analysis. The beam is shown in Figure 3.1.

This comparison also results in an absolute temperature calibration by comparing the SPTpol and *Planck* maps over the multipole range $600 < \ell < 1000$. The actual absolute calibration that we apply comes from allowing the temperature and polarization calibrations to be free parameters when performing cosmological fitting to the EE and TE power spectra of the 500 $\deg^2$ patch in Henning et al. (in prep).

3.7 T to P deprojection

Temperature data will leak into polarization maps if, for instance, the relative gains of a detector pair are incorrectly calibrated, the two detectors' pointing differs slightly, or there is differential ellipticity to the beam. We denote this effect by $T \rightarrow P$ leakage. It results in the presence of a fraction of the temperature map (and possibly its first and second derivatives) in Q and U maps.

We estimate the magnitude of this effect by taking a weighted average over multipole

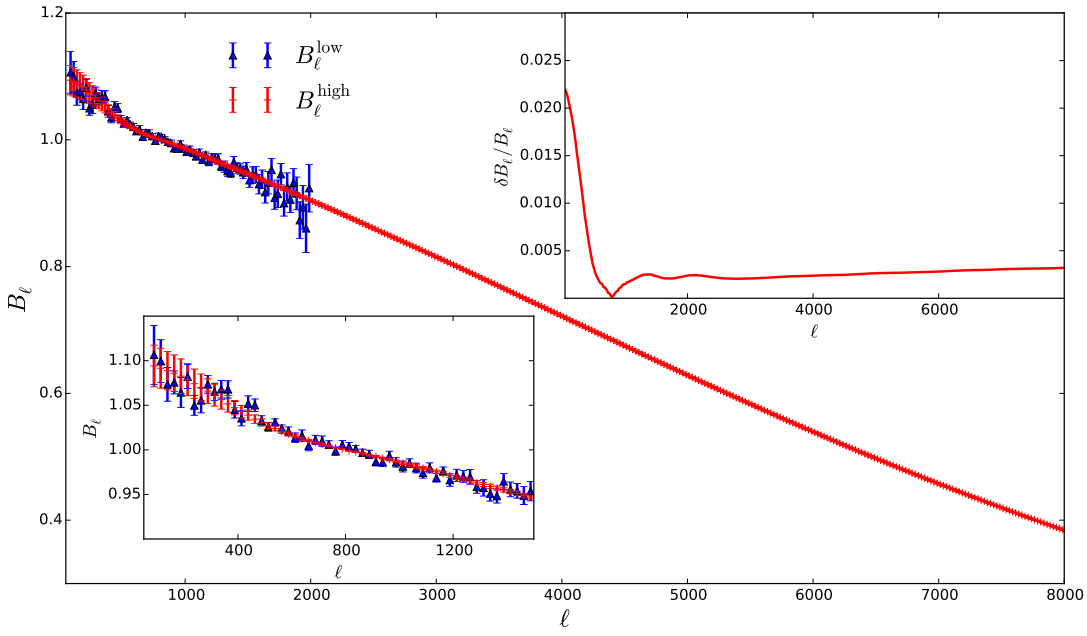

Figure 3.1: The SPTpol beam, from Henning et al. (in prep). The high-ℓ (red) beam is calculated from observations of Venus, and the low-ℓ (blue) part, from cross-correlating *Planck* and SPTpol temperature maps. The lower-left inset shows the agreement between the two calculations, and the higher upper-right inset shows the fractional statistical errors.

space of the cross-correlation of temperature with either Q or U maps. We find leakage factors of $\epsilon^Q = 0.017 \pm 0.001$ and $\epsilon^U = 0.008 \pm 0.001$. We deproject a monopole leakage term from the maps by subtracting a copy of the temperature map scaled by these factors from the Q and U maps, respectively.

3.8 Mask

We apply a mask to the map to downweigh the noisy field edges. We mask bright point sources in the map. We use a $5'$ radius to mask sources detected above 5σ in SPT-SZ data, corresponding to a flux cut of $\sim$6.4 mJy. We use a $10'$ radius for sources detected above 75σ. We also mask galaxy clusters detected above a significance $\xi = 4.5$ in SPT data, using a $5'$ radius. The mask has a tophat shape for both the edges and the sources, because the C-inverse filter described in the next chapter acts as an effective apodization.

The mask is shown in Figure 3.2.

3.9 ℓ-space cuts

We remove modes along the scan direction for $\ell_x < 100$, in order to remove isotropic atmospheric noise and low-frequency readout noise. We also cut all modes with $|\boldsymbol{\ell}| > 3500$. We choose both cuts based on systematic tests described in Chapter 7.

We now have filtered and masked CMB T, Q, and U maps that are ready to be used as input to the lensing pipeline, which we describe in the next chapter.

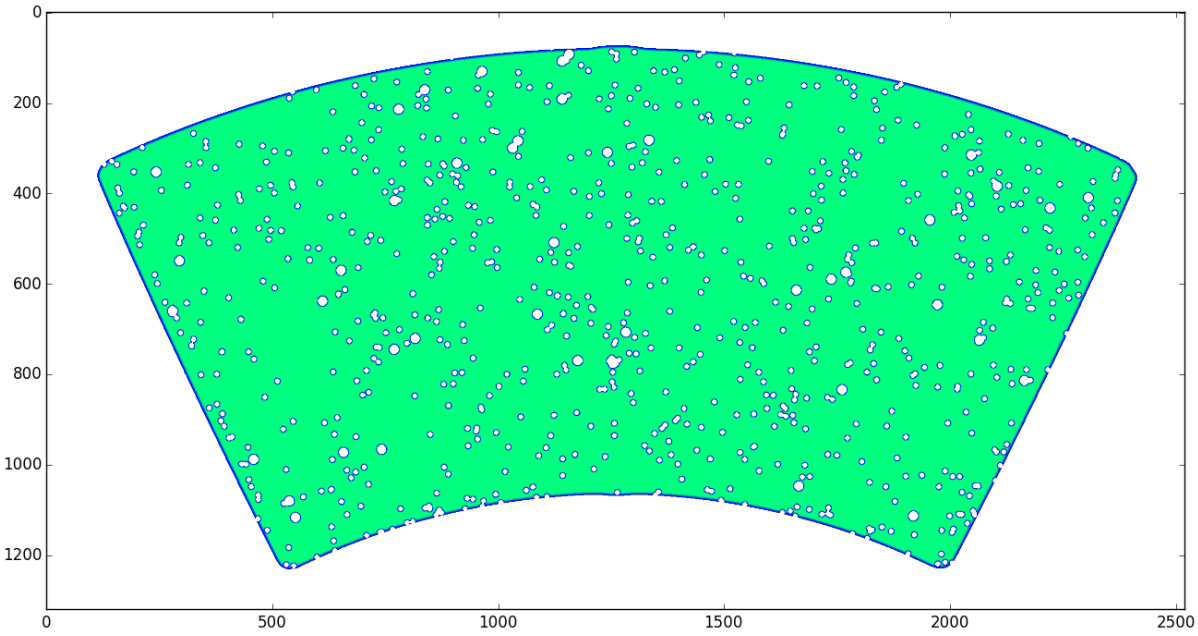

Figure 3.2: Mask applied to the 500 $\deg^2$ field.

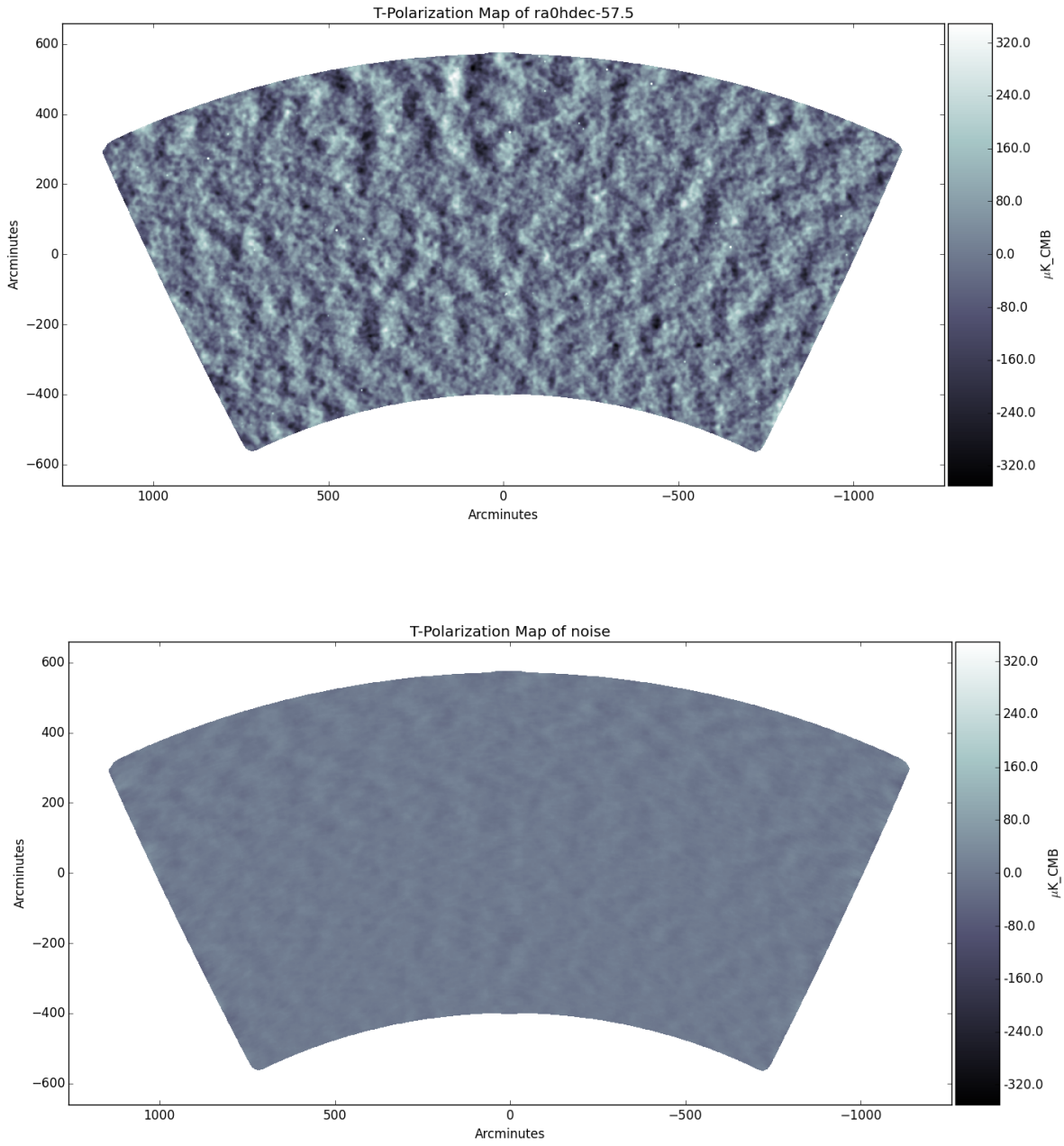

Figure 3.3: Temperature map coadd (top) and difference map (bottom) for the survey field.

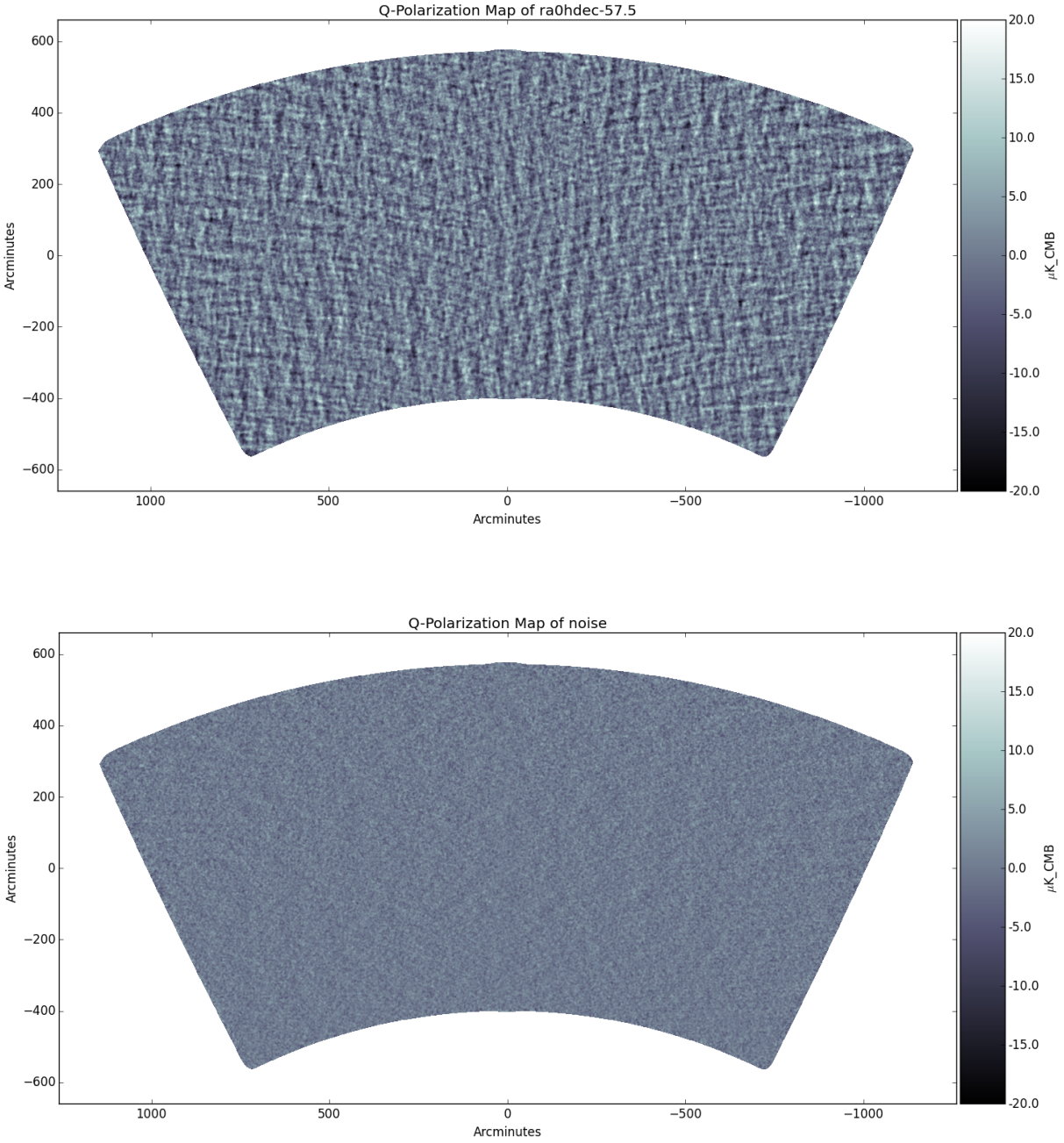

Figure 3.4: Q map coadd (top) and difference map (bottom) for the survey field.

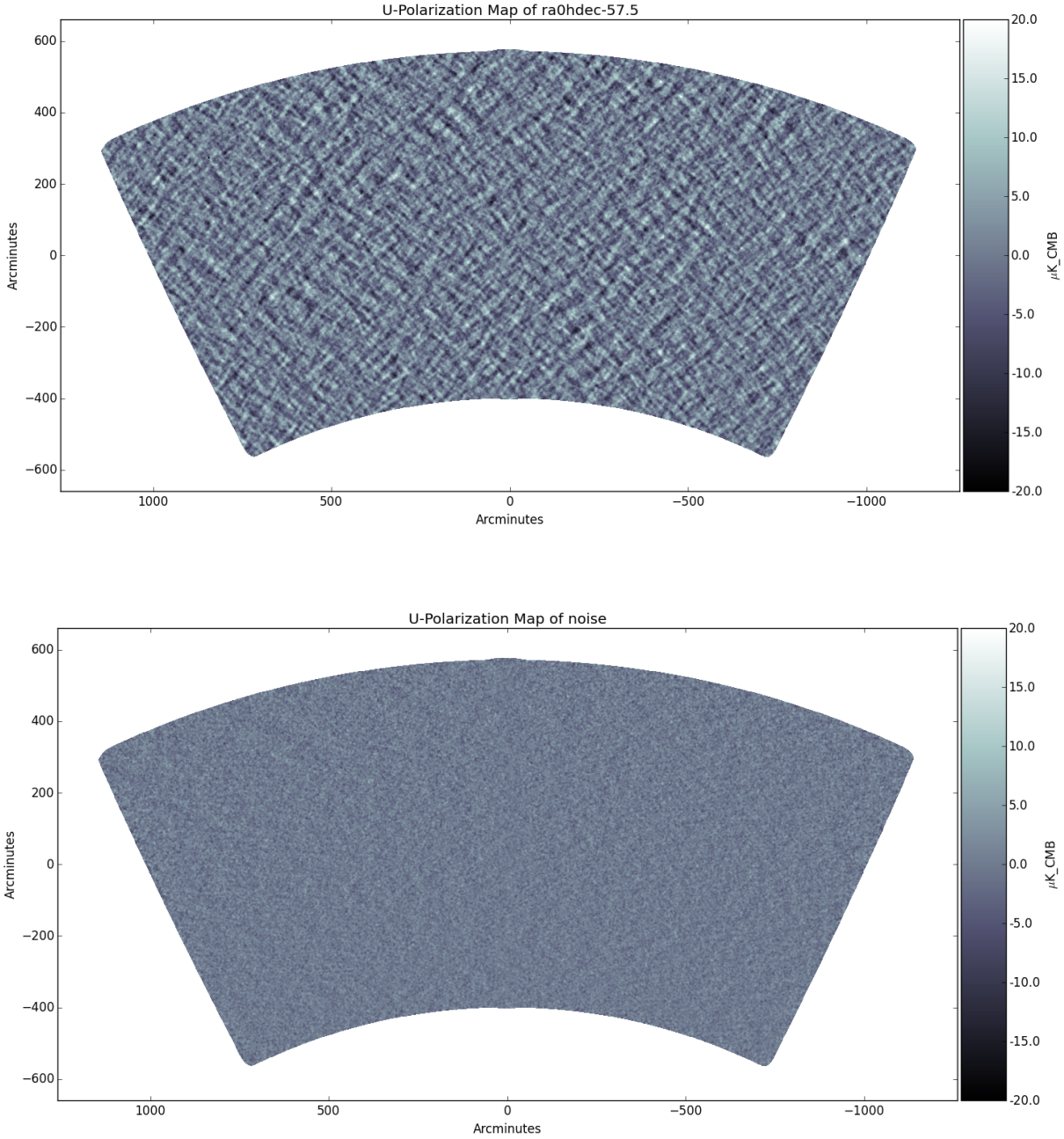

Figure 3.5: U map coadd (top) and difference map (bottom) for the survey field.

CHAPTER 4

CMB LENSING ANALYSIS

Weak lensing by large-scale structure remaps the temperature T and Stokes Q and U CMB fields according to [55, 56, 29]:

$$T(\hat{\mathbf{n}}) = T^{\rm unl}(\hat{\mathbf{n}} + \vec{\alpha}) \tag{4.1}$$

$$[Q \pm iU](\hat{\mathbf{n}}) = [Q^{\rm unl} \pm iU^{\rm unl}](\hat{\mathbf{n}} + \vec{\alpha}), \tag{4.2}$$

where $\hat{\mathbf{n}}$ is a unit vector along the line of sight, and $\vec{\alpha}$ is the deflection angle. We note that we keep to the definitions commonly used in CMB lensing literature, in which the deflection angle $\vec{\alpha}$ points from the lensed towards the unlensed position, opposite to the more standard definition.

A photon at the surface of last scattering is deflected by a three-dimensional gravitational potential Ψ by an angle [4]

$$\vec{\alpha} = -2\int_0^{\chi_{\rm CMB}} d\chi \frac{f_K(\chi_{\rm CMB} - \chi)}{f_K(\chi_{\rm CMB}) f_K(\chi)} \nabla_{\hat{\mathbf{n}}} \Psi(\chi\hat{\mathbf{n}}; \eta_0 - \chi) \tag{4.3}$$

where χ is the comoving distance along the line of sight, $\chi_{\rm CMB}$ is the comoving distance to the surface of last scattering, $\eta_0 - \chi$ is the conformal time at which the photon was at position $\chi\hat{\mathbf{n}}$, and $f_K(\chi)$ is the angular diameter distance, with $f_K(\chi) = \chi$ in a flat universe.

The projected lensing potential $\phi(\hat{\mathbf{n}})$ is defined as an integral along the line of sight of the three-dimensional gravitational potential Ψ:

$$\phi(\hat{\mathbf{n}}) = -2\int_0^{\chi_{\rm CMB}} d\chi \frac{f_K(\chi_{\rm CMB} - \chi)}{f_K(\chi_{\rm CMB}) f_K(\chi)} \Psi(\chi\hat{\mathbf{n}}; \eta_0 - \chi), \tag{4.4}$$

such that $\vec{\alpha} = \nabla\phi(\hat{\mathbf{n}})$. We also note that this definition of the lensing potential (common in CMB lensing literature) implies that ϕ is increasing towards massive structures, which is

opposite to the regular definition of gravitational potential that becomes more negative at mass concentrations.

The convergence field κ is defined as the divergence of $\nabla\phi$:

$$\kappa(\hat{\mathbf{n}}) \equiv -\frac{1}{2}\nabla^2\phi(\hat{\mathbf{n}}). \tag{4.5}$$

and represents the local magnification or demagnification of the CMB.

Equations 4.1 and 4.2 describe linear perturbations at last scattering being weakly lensed by linear perturbations along the line of sight. They are valid assuming assuming weak lensing, i.e., that the deflection angles are small. We describe lensing to the lowest order in the lensing potential and neglect the small, higher order corrections in this analysis. This approximation also implies that the deflection angles have a null curl, since they can be written as the gradient of a potential.

We proceed to describe the filtering of the maps that go into the analysis, the estimation of the lensing potential, its unbiasing and normalization, and the calculation of the lensing power spectrum.

4.1 Map filtering

We filter the maps to improve sensitivity to our signal of interest, the CMB, relative to the noise.

The maps we produce contain CMB and other sources of astrophysical signal (foregrounds) convolved with the telescope beam, filtering, map pixelization, and instrumental noise. The T, Q, U data maps in real space are assumed to be given by the following expression, with j indexing pixel number:

$$d_j = \sum_{\boldsymbol{\ell}} P_{j\boldsymbol{\ell}} X_{\boldsymbol{\ell}} + \sum_{\boldsymbol{\ell}} P_{j\boldsymbol{\ell}} N_{\boldsymbol{\ell}} + n_j \tag{4.6}$$

where $X_{\boldsymbol{\ell}} \in [T_{\boldsymbol{\ell}}, E_{\boldsymbol{\ell}}, B_{\boldsymbol{\ell}}]$, $P_{j\boldsymbol{\ell}}$ is a matrix operator that applies the filtering transfer function, beam and pixelization, $N_{\boldsymbol{\ell}}$ is the sky noise, and n_j is a map-domain noise contribution from instrumental noise.

The two noise components are defined as follows: $N_{\boldsymbol{\ell}}$ comes from foregrounds or atmospheric emission, and n_j is due to instrumental noise and is taken to be white and uncorrelated between pixels. This is not an entirely accurate description, since filtering is applied to instrumental noise as well. We choose this model for convenience and note that it will result in a slighly overestimate of the instrumental variance and cause the filtering to be marginally suboptimal.

Inverse variance filtered modes $\bar{X}$ are given by [57]

$$\left[S^{-1} + P^{\dagger} n^{-1} P\right] S\bar{X} = P^{\dagger} n^{-1} d\,. \tag{4.7}$$

We can solve for the filtered modes $\bar{X}$:

$$\bar{X} = S^{-1}\left[S^{-1} + P^{\dagger} n^{-1} P\right]^{-1} P^{\dagger} n^{-1} d\,, \tag{4.8}$$

where S is the total signal covariance, n^{-1} is the mask multiplied by the inverse map noise variance. We invert the matrix between brackets using the iterative conjugate gradient descent method, as in [31].

We also use an approximation for this filtering process that neglects the mixing of power between different $\boldsymbol{\ell}$ multipoles. In this approximation, the filtered modes can be expressed as:

$$\bar{X}_{\boldsymbol{\ell}} \approx \mathcal{F}^{X}_{\boldsymbol{\ell}} X_{\boldsymbol{\ell}} + n^{X}_{\boldsymbol{\ell}} \tag{4.9}$$

where $\mathcal{F}^{X}_{\boldsymbol{\ell}}$ is the filter function. By approximating all the operators in Equation 4.8 as

diagonal, we arrive at the form

$$\mathcal{F}^X_{\boldsymbol{\ell}} X_{\boldsymbol{\ell}} \equiv [C^{XX}_{\boldsymbol{\ell}} + C^{NN}_{\boldsymbol{\ell}}]^{-1} X_{\boldsymbol{\ell}}, \tag{4.10}$$

where $C^{XX}_{\boldsymbol{\ell}}$ is the power spectrum of the field X and $C^{NN}_{\boldsymbol{\ell}}$ is the map noise power spectrum. We use the full filtering process described in this section to filter the CMB fields, and we only use this diagonal approximation to analytically compute the normalization of the lensing estimator, described in Section 4.2.3 (and for one consistency test).

The filtered $\bar{T}, \bar{E}, \bar{B}$ fields are then fed into the quadratic estimator for lensing that we describe below. Cutouts of the filtered maps are shown in Figure 4.1.

4.2 Quadratic estimator of the lensing potential

4.2.1 The estimator

The unlensed CMB is, to a good approximation, a statistically isotropic Gaussian random field, and modes with different multipole $\boldsymbol{\ell}$ are uncorrelated:

$$\langle X^{\rm unl}_{\boldsymbol{\ell}} Y^{\rm unl*}_{\boldsymbol{\ell'}} \rangle = \delta(\boldsymbol{\ell} - \boldsymbol{\ell'}) C^{XY}_{\ell} \tag{4.11}$$

where $X^{\rm unl}$, $Y^{\rm unl}$ are unlensed CMB fields.

Lensing introduces off-diagonal correlations between CMB modes. We use a quadratic estimator to measure these correlations and reconstruct the lensing potential [12]. The expression for the quadratic estimator is:

$$\bar{\phi}^{XY}_{\mathbf{L}} = \int d^2\boldsymbol{\ell} W^{XY}_{\boldsymbol{\ell},\boldsymbol{\ell}-\mathbf{L}} \bar{X}_{\boldsymbol{\ell}} \bar{Y}^*_{\boldsymbol{\ell}-\mathbf{L}} \tag{4.12}$$

where $\bar{X}$ and $\bar{Y}$ are filtered T, E or B fields, W is a weight function, $\boldsymbol{\ell}$ are modes in the

CMB and $\mathbf{L}$ are modes in the lensing potential.

This estimator is a weighted sum of off-diagonal elements in the covariance between modes $\boldsymbol{\ell}$ in field X and modes $\boldsymbol{\ell} - \mathbf{L}$ in field Y. The amount of lensing on scale $\mathbf{L}$ is thus an average over CMB modes separated by this scale. In other words, we use correlations between many anisotropies around a lens to constrain the potential of the lens.

Holding the lensing potential fixed and averaging over different realizations of the CMB fields, the latter can be expanded in a Taylor series as a function of ϕ [12]:

$$\langle X_{\boldsymbol{\ell}}\, Y^*_{\boldsymbol{\ell}'}\rangle_{\rm CMB} = \delta(\boldsymbol{\ell}-\boldsymbol{\ell}')C_l^{XY} + \mathcal{W}^{\phi XY}_{\boldsymbol{\ell},\boldsymbol{\ell}'}\,\phi_{\boldsymbol{\ell}-\boldsymbol{\ell}'} + \mathcal{O}(\phi^2)\,. \tag{4.13}$$

The zeroth order term in the expansion is the regular two point correlation or power spectrum corresponding to a Gaussian random field. The lensing information is contained in the first and higher order terms in this expansion. In this analysis, we neglect the second and higher order terms.

One can construct different types of quadratic estimators. The type is determined by the choice of weight function $W^{\phi XY}_{\boldsymbol{\ell},\boldsymbol{\ell}-\mathbf{L}}$ in Equation 4.12. We use the minumum-variance estimator, where the weight is defined to be the leading-order coefficient of ϕ in the expansion in Equation 4.13, $W^{XY}_{\boldsymbol{\ell},\boldsymbol{\ell}-\mathbf{L}} = \mathcal{W}^{\phi XY}_{\boldsymbol{\ell},\boldsymbol{\ell}'}$. This weight is a matched filter for the covariance induced by lensing. The weight functions for every XY estimator are given in [12]. One can also choose to use other estimators, such as "bias-hardened" estimators [58] whose weight functions are orthogonal to systematic effects such as foregrounds.

We use CMB modes between multipoles $100 < \ell < 3500$. Most of the lensing information comes from arcminute CMB scales, while the lensing potential peaks on degree scales. In other words, we use arcminute CMB scales to reconstruct the lensing potential on degree scales.

4.2.2 Mean-field bias

After calculating this estimate $\bar{\phi}$, we need to unbias and normalize it. The estimator is biased due to contributions from other sources of statistical anisotropy, such as the sky mask or inhomogeneous map noise. We construct and subtract a mean-field (MF) bias using 100 simulations that have different realizations of CMB skies, lensing potential and noise:

$$\bar{\phi}^{XY,\mathrm{MF}}_{\mathbf{L}} = \int d^2\boldsymbol{\ell} W^{XY}_{\boldsymbol{\ell},\boldsymbol{\ell}-\mathbf{L}} \langle \bar{X}_{\boldsymbol{\ell}} \bar{Y}^*_{\boldsymbol{\ell}-\mathbf{L}} \rangle \,, \tag{4.14}$$

The production of those simulations is described in Chapter 5. Because we average over independent $\bar{X}$, $\bar{Y}$ realizations, the lensing signal averages out of the expression above and the remaining part is just the MF bias.

4.2.3 Normalization

After subtracting the MF bias, we normalize the estimator by a $\mathcal{R}^{XY}_{\mathbf{L}}$ factor:

$$\hat{\phi}^{XY}_{\mathbf{L}} = \frac{1}{\mathcal{R}^{XY}_{\mathbf{L}}} (\bar{\phi}^{XY}_{\mathbf{L}} - \bar{\phi}^{XY,\mathrm{MF}}_{\mathbf{L}}) \,. \tag{4.15}$$

The normalization factor $\mathcal{R}^{XY}_{\mathbf{L}}$ is a combination of an analytic normalization and a simulation-based correction:

$$\mathcal{R}^{XY}_{\mathbf{L}} \equiv \mathcal{R}^{XY,\ \mathrm{Analytic}}_{\mathbf{L}} \times \mathcal{R}^{XY,\mathrm{MC}}_{L} \,. \tag{4.16}$$

To calculate the analytic normalization, we approximate the C-inverse filter as diagonal in Fourier space, as described in the previous section. This analytical normalization is given by

$$\mathcal{R}^{XY,\mathrm{Analytic}}_{\mathbf{L}} = \int d^2\boldsymbol{\ell}\, W^{XY}_{\boldsymbol{\ell},\boldsymbol{\ell}-\mathbf{L}} \times \mathcal{W}^{\phi^{XY}}_{\boldsymbol{\ell},\boldsymbol{\ell}-\mathbf{L}} \mathcal{F}^X_\ell \mathcal{F}^Y_{\boldsymbol{\ell}-\mathbf{L}} \,. \tag{4.17}$$

Because this diagonal approximation is not exact, we calculate a correction to the normalization from simulations:

$$\mathcal{R}_{\mathbf{L}}^{XY,\mathrm{MC}} = \frac{\langle \hat{\phi}_{\mathbf{L}}^{I',XY} \; \phi_{\mathbf{L}}^{I*} \rangle}{\langle \phi_{\mathbf{L}}^{I} \phi_{\mathbf{L}}^{I*} \rangle} \,, \tag{4.18}$$

where $\phi_{\mathbf{L}}^{I}$ is the input lensing potential for a given simulation and $\hat{\phi}^{I',XY}$ is the reconstructed potential for that simulation using the lensing pipeline, namely:

$$\hat{\phi}_{\mathbf{L}}^{I',XY} = \frac{1}{\mathcal{R}_{\mathbf{L}}^{XY,\mathrm{Analytic}}} (\bar{\phi}_{\mathbf{L}}^{XY} - \bar{\phi}_{\mathbf{L}}^{XY,\mathrm{MF}}) \tag{4.19}$$

The total normalization is thus the product of the two,

$$\mathcal{R}_{\mathbf{L}}^{XY} \equiv \mathcal{R}_{\mathbf{L}}^{XY,\mathrm{Analytic}} \times \mathcal{R}_{L}^{XY,\mathrm{MC}} \,. \tag{4.20}$$

where $\mathcal{R}_{\mathbf{L}}^{XY,\mathrm{MC}}$ has been averaged over annuli in $\mathbf{L}$-space to form $\mathcal{R}_{L}^{XY,\mathrm{MC}}$ in order to reduce noise present in the full 2D object.

4.2.4 Combining the estimators

We construct all of the individual estimators $XY \in [TT, TE, EE, EB, TB]$. The BB estimator has null signal-to-noise in our analysis if we assume negligible primordial B-mode power. The B-mode power is coming from lensed E-modes and is at most first order in ϕ, which means that the BB estimator will only be second order in ϕ and negligible in our approximation.

We combine the five estimators into a minimum variance estimator, $\hat{\phi}_{\mathbf{L}}^{\mathrm{MV}}$, by taking a weighted average:

$$\hat{\phi}_{\mathbf{L}}^{\mathrm{MV}} = \frac{\sum_{XY} w_{\mathbf{L}}^{XY} \hat{\phi}_{\mathbf{L}}^{XY}}{\sum_{XY} w_{\mathbf{L}}^{XY}} \,, \tag{4.21}$$

where the weight $w_{\mathbf{L}}^{XY} = \mathcal{R}_{\mathbf{L}}^{XY}$.

We also construct a polarization-only estimator, $\hat{\phi}_{\mathbf{L}}^{\mathrm{POL}}$, using just the EE and EB esti-

mators.

4.3 The power spectrum of the lensing potential

We now wish to calculate a power spectrum of the potential estimate described above. We do this by first calculating a cross-spectrum of two estimates of ϕ, subtracting two noise bias terms, RDN0 and N1 (described below), binning the spectrum, and then calculating the amplitude of the spectrum relative to a theory spectrum. We detail all of those steps in this section.

We start by computing a cross-spectrum between two estimates of the lensing potential, $\hat{\phi}^{UV}$ and $\hat{\phi}^{XY}$:

$$C_{\mathbf{L}}^{\hat{\phi}^{UV}\hat{\phi}^{XY}} \equiv f_{\text{mask}}^{-1}\langle \hat{\phi}_{\mathbf{L}}^{UV}\ \hat{\phi}^{*}{}_{\mathbf{L}}^{XY}\rangle\,, \tag{4.22}$$

where f_{mask} is the average value of the fourth power of the mask applied to the field. For each of the two $\hat{\phi}$ estimates, we compute the mean-field bias from two separate sets of simulations in order to eliminate any correlations due to noise.

4.3.1 Bias terms

This power spectrum is biased. We therefore compute and subtract two additive noise bias terms, RDN0 and N1 [12, 59].

The N0 bias is Gaussian noise bias due to correlations between the CMB, foregrounds and noise. It comes from disconnected contributions to the four-point function and has a large magnitude. This bias term would be present even in the absence of lensing. We calculate it from two sets of simulations with different realizations of CMB sky, lensing potential, and

foregrounds:

$$\Delta C_{\mathbf{L}}^{\phi\phi}\Big|_{\mathrm{N0}} = \Big\langle \quad C_{\mathbf{L}}^{\hat{\phi}\hat{\phi}}[\bar{U}_i^{\phi_i}, \bar{V}_j^{\phi_j}, \bar{X}_i^{\phi_i}, \bar{Y}_j^{\phi_j}] + C_{\mathbf{L}}^{\hat{\phi}\hat{\phi}}[\bar{U}_i^{\phi_i}, \bar{V}_j^{\phi_j}, \bar{X}_j^{\phi_j}, \bar{Y}_i^{\phi_i}] \quad \Big\rangle_{i,j} \tag{4.23}$$

where $\bar{U}_i^{\phi_1}$ is the i-th simulated $\bar{T}$, $\bar{E}$ or $\bar{B}$ lensed field with lensing potential realization ϕ_i and i, j index different simulation realizations.

There will be some difference between the power spectrum of the data and the theoretical spectrum that we use as input to the simulations. To minimize the effects of this difference, we calculate a realization-dependent N0 bias (RDN0) [58] by replacing one of the simulated CMB fields with the data:

$$\begin{aligned}\Delta C_{\mathbf{L}}^{\phi\phi}\Big|_{\mathrm{RDN0}} = \Big\langle \quad & C_{\mathbf{L}}^{\hat{\phi}\hat{\phi}}[\bar{U}_{\mathrm{d}}, \bar{V}_i^{\phi_i}, \bar{X}_{\mathrm{d}}, \bar{Y}_i^{\phi_i}] \\ & + C_{\mathbf{L}}^{\hat{\phi}\hat{\phi}}[\bar{U}_i^{\phi_i}, \bar{V}_{\mathrm{d}}, \bar{X}_{\mathrm{d}}, \bar{Y}_i^{\phi_i}] \\ & + C_{\mathbf{L}}^{\hat{\phi}\hat{\phi}}[\bar{U}_{\mathrm{d}}, \bar{V}_i^{\phi_i}, \bar{X}_i^{\phi_i}, \bar{Y}_{\mathrm{d}}] \\ & + C_{\mathbf{L}}^{\hat{\phi}\hat{\phi}}[\bar{U}_i^{\phi_i}, \bar{V}_{\mathrm{d}}, \bar{X}_i^{\phi_i}, \bar{Y}_{\mathrm{d}}] \\ & - C_{\mathbf{L}}^{\hat{\phi}\hat{\phi}}[\bar{U}_i^{\phi_i}, \bar{V}_j^{\phi_j}, \bar{X}_i^{\phi_i}, \bar{Y}_j^{\phi_j}] \\ & - C_{\mathbf{L}}^{\hat{\phi}\hat{\phi}}[\bar{U}_i^{\phi_i}, \bar{V}_j^{\phi_j}, \bar{X}_j^{\phi_i}, \bar{Y}_i^{\phi_j}] \quad \Big\rangle_{i,j},\end{aligned} \tag{4.24}$$

where the d subscript stands for data. This bias correction is constructed in such a way that it is insensitive to differences between the power spectrum of the data and of the simulations to first order, which makes it robust despite its large magnitude relative to the signal.

The N1 bias is linear in the lensing potential power spectrum $C_L^{\phi\phi}$ and emerges due to connected contributions (secondary contractions) of the two lensing potential fields to the four-point function [59]. We calculate it using simulations that have the same realizations

of the lensing potential ϕ and different realizations of CMB skies, as follows:

$$\begin{aligned}\Delta C_{\mathbf{L}}^{\phi\phi}\Big|_{\mathrm{N1}} = \Big\langle \quad & C_{\mathbf{L}}^{\hat{\phi}\hat{\phi}}[\bar{U}_i^{\phi^i}, \bar{V}_j^{\phi^i}, \bar{X}_i^{\phi^i}, \bar{Y}_j^{\phi^i}] \\ & + C_{\mathbf{L}}^{\hat{\phi}\hat{\phi}}[\bar{U}_i^{\phi^i}, \bar{V}_j^{\phi^i}, \bar{X}_j^{\phi^i}, \bar{Y}_i^{\phi^i}] \\ & - \Delta C_{\mathbf{L}}^{\phi\phi}\Big|_{\mathrm{N0}} \quad \Big\rangle_{i,j},\end{aligned} \tag{4.25}$$

The simulations used for the N1 calculation contain only homogeneous map noise and no foregrounds.

We see a small difference between the mean reconstructed lensing spectrum from 400 simulations and the input used to produce those simulations. This can be due to errors in normalizing the spectrum, in calculating the N1 bias, mode-mixing, leakage effects from masking (correlations beyond the mean-field), or higher order corrections, and other groups report a similar issue [5, 7]. Since the effect is small and its origin is not obvious, we can treat it as either an additive or multiplicative term and correct for it. We plan to treat it as an additive correction, which we denote by $\Delta C_{\mathbf{L}}^{\phi\phi}\Big|_{\mathrm{MC}}$. This is discussed more in Chapter 7.

We obtain the spectrum by subtracting these two noise bias terms and the MC correction from the initial estimate:

$$\hat{C}_{\mathbf{L}}^{\phi\phi} = C_{\mathbf{L}}^{\hat{\phi}\hat{\phi}} - \Delta C_{\mathbf{L}}^{\phi\phi}\Big|_{\mathrm{RDN0}} - \Delta C_{\mathbf{L}}^{\phi\phi}\Big|_{\mathrm{N1}} - \Delta C_{\mathbf{L}}^{\phi\phi}\Big|_{\mathrm{MC}}. \tag{4.26}$$

4.3.2 Binning

The $\hat{C}_{\mathbf{L}}^{\phi\phi}$ is a two-dimensional quantity. We bin this spectrum into a one-dimensional object. We calculate a weighted average of $\hat{C}_{\mathbf{L}}^{\phi\phi}$ in a bin b:

$$C_b^{\phi^{UV}\phi^{XY}} \equiv \frac{\sum_{\mathbf{L}\in b} w_{\mathbf{L}}^{UVXY} \hat{C}_{\mathbf{L}}^{\phi^{UV}\phi^{XY}}}{\sum_{\mathbf{L}\in b} w_{\mathbf{L}}^{UVXY}} \tag{4.27}$$

using weights $w_{\mathbf{L}}^{UVXY} = \mathcal{R}_{\mathbf{L}}^{UV}\mathcal{R}_{\mathbf{L}}^{XY}$. $\mathcal{R}_{\mathbf{L}}^{XY}$ is the Fisher matrix for $\phi_{\mathbf{L}}$, such that the normalization matrix is the covariance matrix of the lensing reconstruction. The unnormalized lensing estimate, $\bar{\phi}_{\mathbf{L}}^{XY} - \bar{\phi}_{\mathbf{L}}^{XY,\mathrm{MF}}$, is thus an inverse-variance weighted lensing reconstruction.

We calculate the amplitude of the data spectrum in a bin b relative to a theory spectrum:

$$A_b^{UVXY} \equiv \frac{C_b^{\phi^{UV}\phi^{XY}}}{C_b^{\phi^{UV}\phi^{XY},\mathrm{theory}}}\,, \tag{4.28}$$

with the theory spectrum

$$C_b^{\phi^{UV}\phi^{XY},\mathrm{theory}} \equiv \frac{\sum_{\mathbf{L}\in b} w_{\mathbf{L}}^{UVXY} C_{\mathbf{L}}^{\phi\phi,\mathrm{theory}}}{\sum_{\mathbf{L}\in b} w_{\mathbf{L}}^{UVXY}}\,. \tag{4.29}$$

We choose as the theory spectrum the best-fit ΛCDM model to the *Planck* `plikHM_TT_lowTEB_lensing` dataset [5], which includes the low-ℓ temperature and polarization and the lensing power spectrum reconstruction.

The bandpowers we report in a bin b with center L_b are the amplitudes A_b multiplied by the theoretical spectrum (averaged) in the bin:

$$\hat{C}_{L_b}^{\phi\phi} \equiv A_b C_{L_b}^{\phi\phi,\mathrm{theory}}\,. \tag{4.30}$$

We also calculate an overall amplitude of $C_L^{\phi\phi}$ relative to the theory spectrum by choosing a single bin that spans the entire L range.

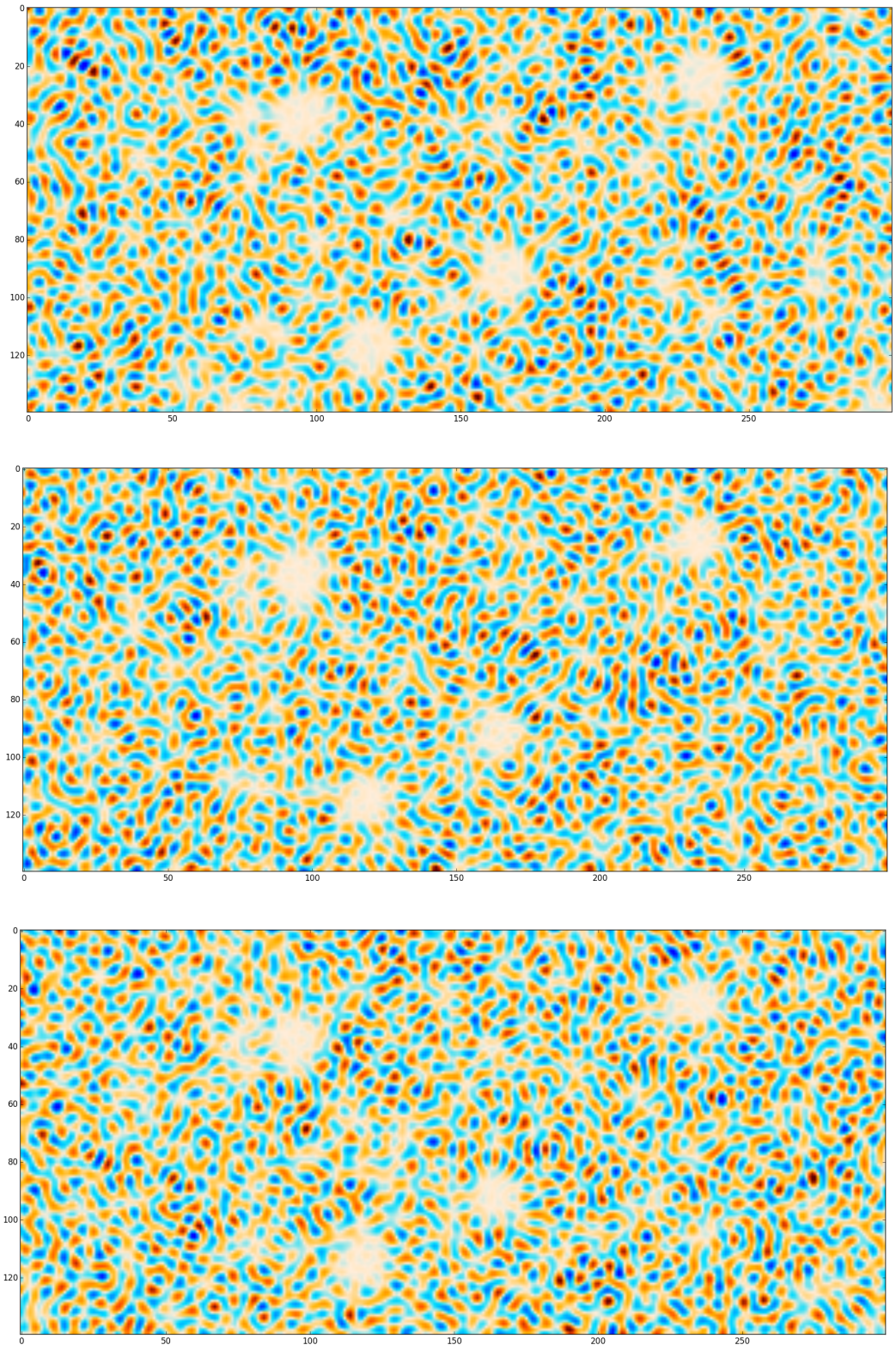

Figure 4.1: Cutouts of the filtered T (top), E (middle), and B (bottom) maps, after C-inverse filtering.

CHAPTER 5

SIMULATIONS

The lensing pipeline uses simulations for multiple purposes. Simulations contain CMB signal, foregrounds, and instrumental noise. We outline their creation and use below.

5.1 Procedure

We start by describing how we produce our set of simulated maps. We generate realizations of T, E, and B simulated skies in HealPix [60] format using LensPix [61] and realizations of a lensing potential. The skies have $N_{side} = 8192$. We use the best-fit ΛCDM model to the *Planck* `plikHM_TT_lowTEB_lensing` dataset as our input theory spectrum. We take the T, E, and B maps and lensing potentials ϕ and convert them to spherical harmonic coefficients a_{lm}. We evaluate the spherical harmonic transform of the a_{lm} coefficients on an equidistant cylindrical projection (ECP) grid.

Next, we add Gaussian realizations of foreground power to the resulting CMB T, E, and B maps, with the following components:

1. dusty star-forming galaxies that make up the cosmic infrared background (CIB): we consider a Poisson-distributed component with $D_\ell \propto \ell^2$ and a clustered component with $D_\ell \propto \ell^{0.8}$,
2. radio galaxies: Poisson-distributed,
3. thermal and kinetic Sunyaev-Zel'dovich (tSZ and kSZ) power, with a model shape from [62], and
4. galactic dust with $D_\ell \propto \ell^{-0.42}$.

Here $D_\ell = \frac{1}{2\pi}\ell(\ell+1)C_\ell$. The amplitudes by which we scale these model components are given below. The amplitudes for tSZ, kSZ, and CIB components are taken from [21], which has the

same source masking threshold as this work. We use an amplitude $D_{\ell=3000}^{\mathrm{tSZ+kSZ}} = 5.66\ \mu K^2$ for the sum of tSZ and kSZ components in temperature maps. We use $D_{\ell=3000}^{\mathrm{radio}} = 1.06\ \mu K^2$ for the Poisson radio component. We use $D_{\ell=3000}^{\mathrm{CIB},P} = 9.16\ \mu K^2$ for the Poisson CIB component and $D_{\ell=3000}^{\mathrm{CIB},cl} = 3.46\ \mu K^2$ for the clustered CIB. We assume a 2% polarization fraction for all the Poisson-distributed (unclustered) components to model extragalatic polarized emission. We use the same model for polarized galactic dust as in [50], with an amplitude $D_{\ell=80}^{\mathrm{TT},dust} = 1.15\ \mu K^2$, $D_{\ell=80}^{\mathrm{EE},dust} = 0.0236\ \mu K^2$, and $D_{\ell=80}^{\mathrm{BB},dust} = 0.0118\ \mu K^2$, where the EE dust amplitude is twice the BB one.

We convolve the resulting skies with the instrumental beam. We then mock-observe these skies with the SPTpol mapmaking pipeline, using the pointing and filtering from real observations. This means that we create mock time-ordered data from these maps for each detector, that are then filtered and binned into maps like the real data. Maps for one mock-obseved simulation are shown in Figures 5.1 and 5.2.

We generate realization of noise from the data. For every observation, we subtract the leftgoing map from the rightgoing map to obtain a so-called difference map. We randomly divide the difference maps into two equal sets. The maps from each set are all coadded together, and then one half-coadd is subtracted from the other. This produces one realization of noise. The sky signal cancels out, leaving the atmospheric and instrumental noise. We generate 500 independent realizations by reshuffling the maps into two different halves each time. We add a different realization of noise to every sky realization.

5.2 Simulation sets

We generate 4 sets of simulations on the NERSC [1] Edison computing cluster:

A. 500 lensed simulations

1. The National Energy Research Scientific Computing Center (NERSC) is the primary scientific computing facility for the Office of Science in the U.S. Department of Energy and is a division of Lawrence Berkeley National Laboratory, located in Berkeley, Calif.

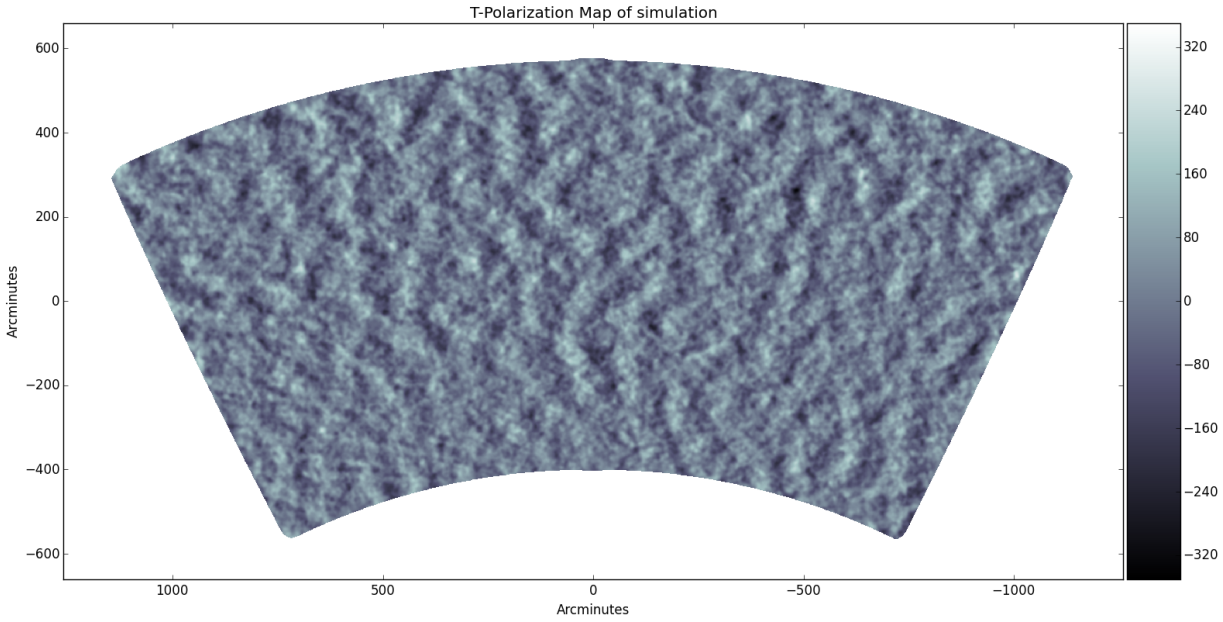

Figure 5.1: Temperature map for one simulated realization. It includes a simulated lensed sky, foregrounds, smoothing by the instrumental beam, and scanning and filtering like the real data.

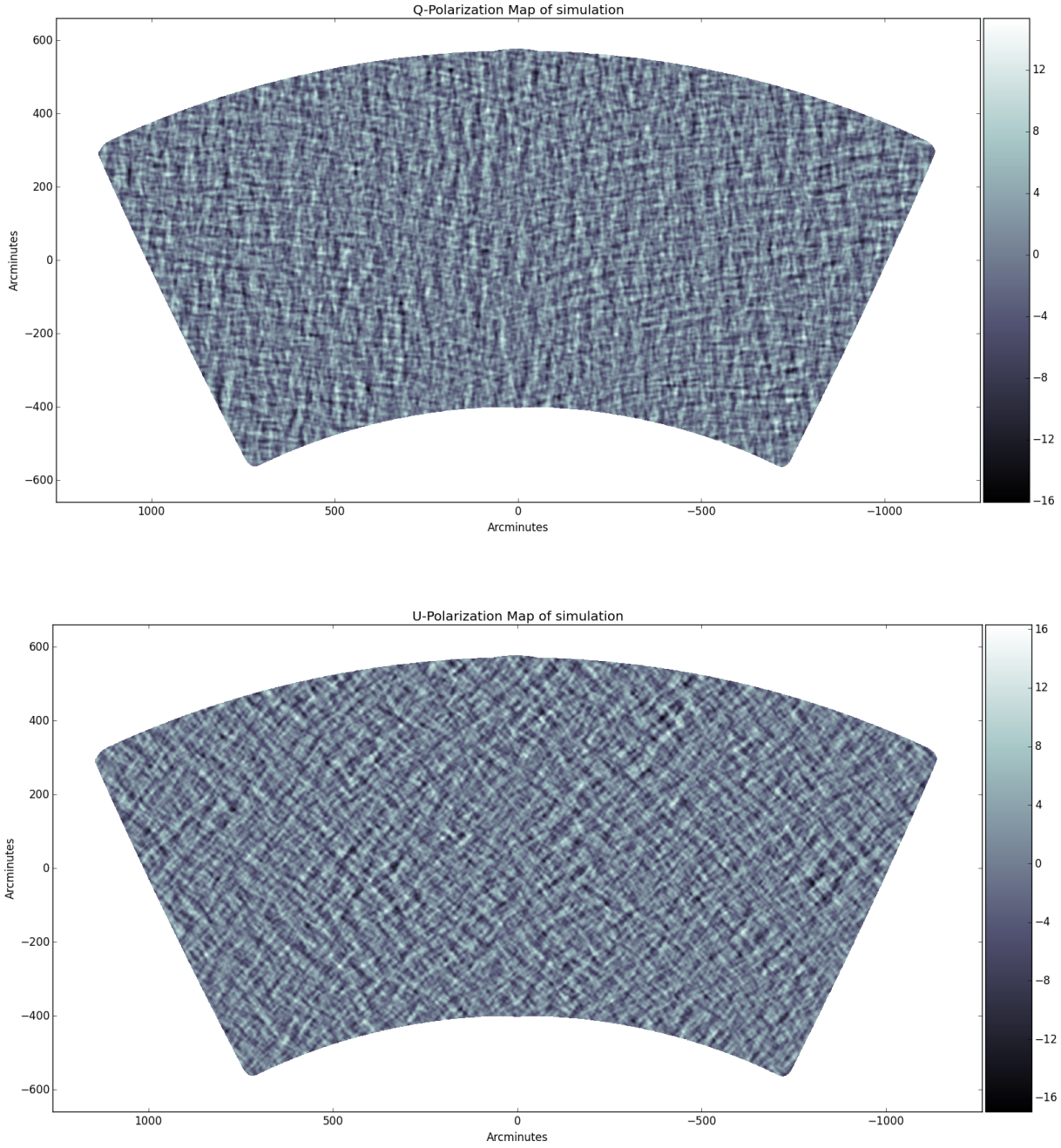

Figure 5.2: Q and U maps of one simulated realization.

B. 500 unlensed simulations

C. 100 lensed simulations without foregrounds

D. 100 lensed simulations without foregrounds with the same realizations of the lensing potential as the simulation in set C, but different CMB realizations.

Set A consists of lensed simulation that include CMB skies, foregrounds, and noise realizations. All 500 simulations are used to calculate the N0 and RDN0 bias terms. 100 of those simulations are used to calculate the mean-field. We divide those 100 simulations into two halves and use 50 for the mean field of the first estimator and the other 50 for the mean field of the second estimator that goes into a power spectrum. The other 400 are used to obtain the statistical uncertainty on the lensing spectrum.

Set B is used to check that the pipeline recovers a spectrum consistent with zero for unlensed skies. The variance among those simulations is also used to quantify the rejection significance of the no-lensing hypothesis, as will be explained in the next chapter.

Sets C and D contain CMB skies and homogeneous (Gaussian) noise realizations, instead of noise realizations obtained from data. The two sets are used together to calculate the N1 bias term.

5.3 Lensing reconstruction from simulations

We show the reconstructed lensing potential from a simulation in the form of a κ map in Figure 5.3. The reconstruction is visually similar to the input lensing potential used to create the simulation.

We show the lensing power spectrum of the lensed and unlensed simulations for the MV estimator, which combines all of the temperature and polarization information, in Figure 5.4. We recover an average amplitude of $A_{\rm len} = 0.961 \pm 0.054$ from the lensed simulations. There is a small difference between the input and recovered spectrum at low L, that we

have referred to as MC bias in the previous chapter, whose amplitude is 3.8% over the full L range. We choose to correct the data for this difference as an additive term.

We recover an amplitude $A_{\rm unl} = -0.002 \pm 0.023$ for the unlensed simulations, confirming that we do not detect any spurious lensing with the pipeline. We also show the simulation lensing power spectra for 16 estimators in Figure 5.5.

We show the distribution of lensing amplitudes reconstructed from simulations in Figure 5.6. This distribution will be used in the next chapter to quantify the significance of the lensing detection in the data and the measurement precision.

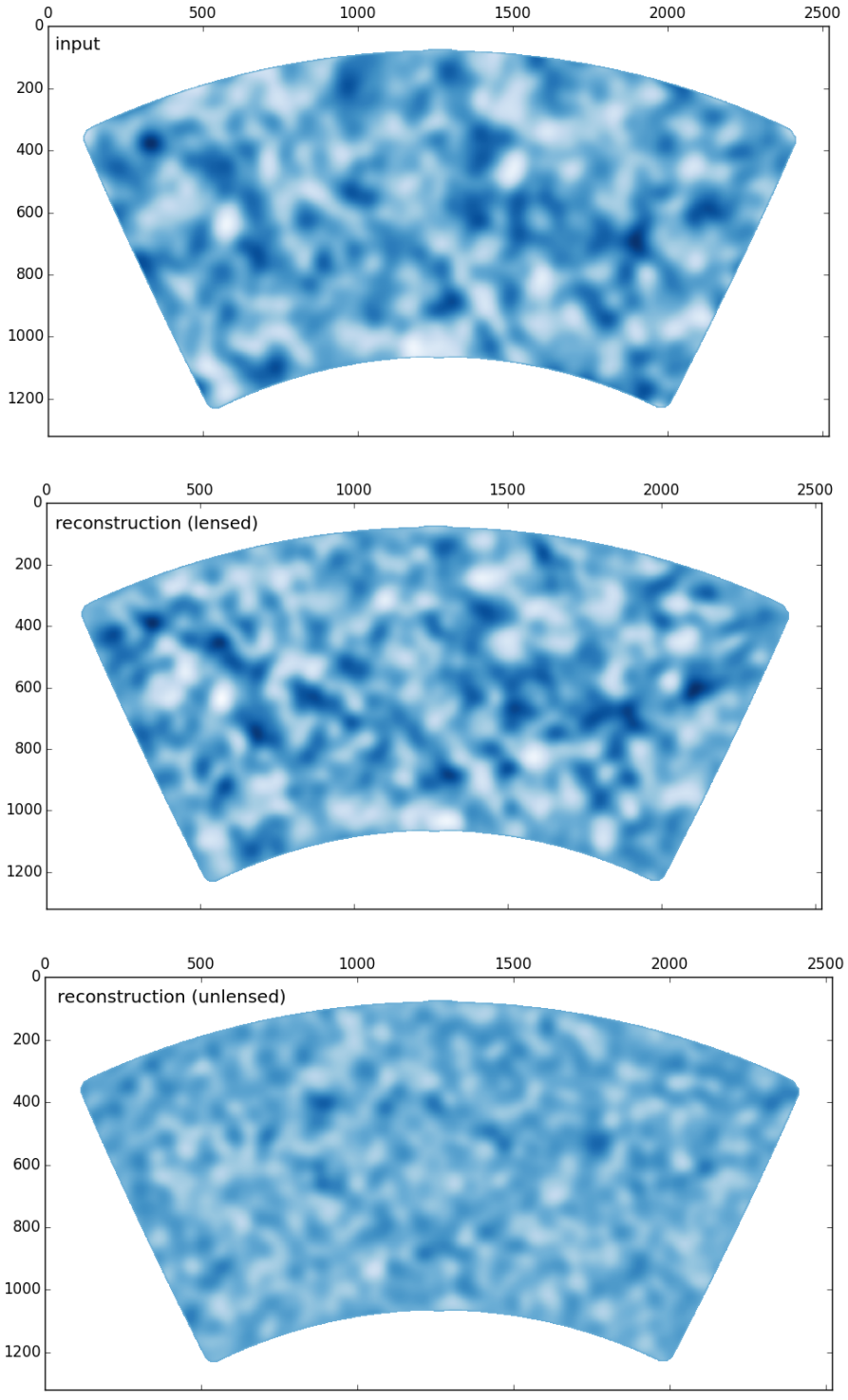

Figure 5.3: A simulated κ map. Top: a realization of an input lensing potential κ-map. Middle: the κ map reconstructed from a simulation that has been lensed using the potential from the top panel. Bottom: the κ map reconstructed from an unlensed simulation. The reconstruction looks visually similar to the input map, and the unlensed reconstruction gives a sense of the noise level.

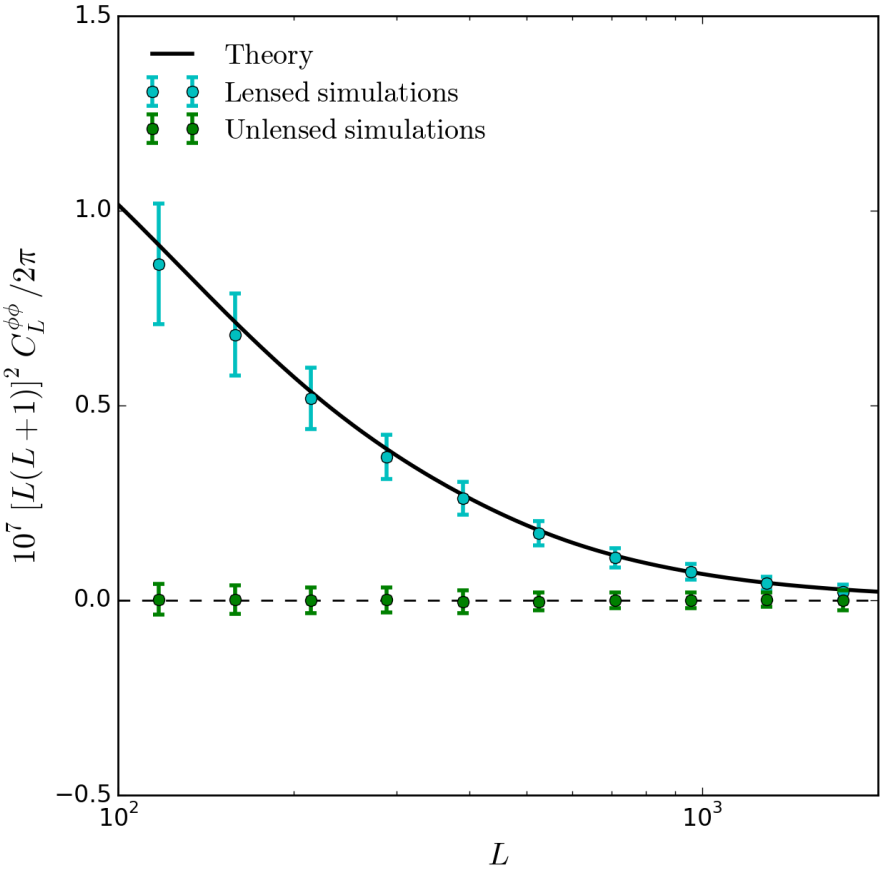

Figure 5.4: Power spectrum of the lensing potential reconstructed from 400 lensed and 400 unlensed simulations, shown for the MV estimator. The theory curve shows the best-fit model to *Planck*data, which is the input spectrum to the simulations.

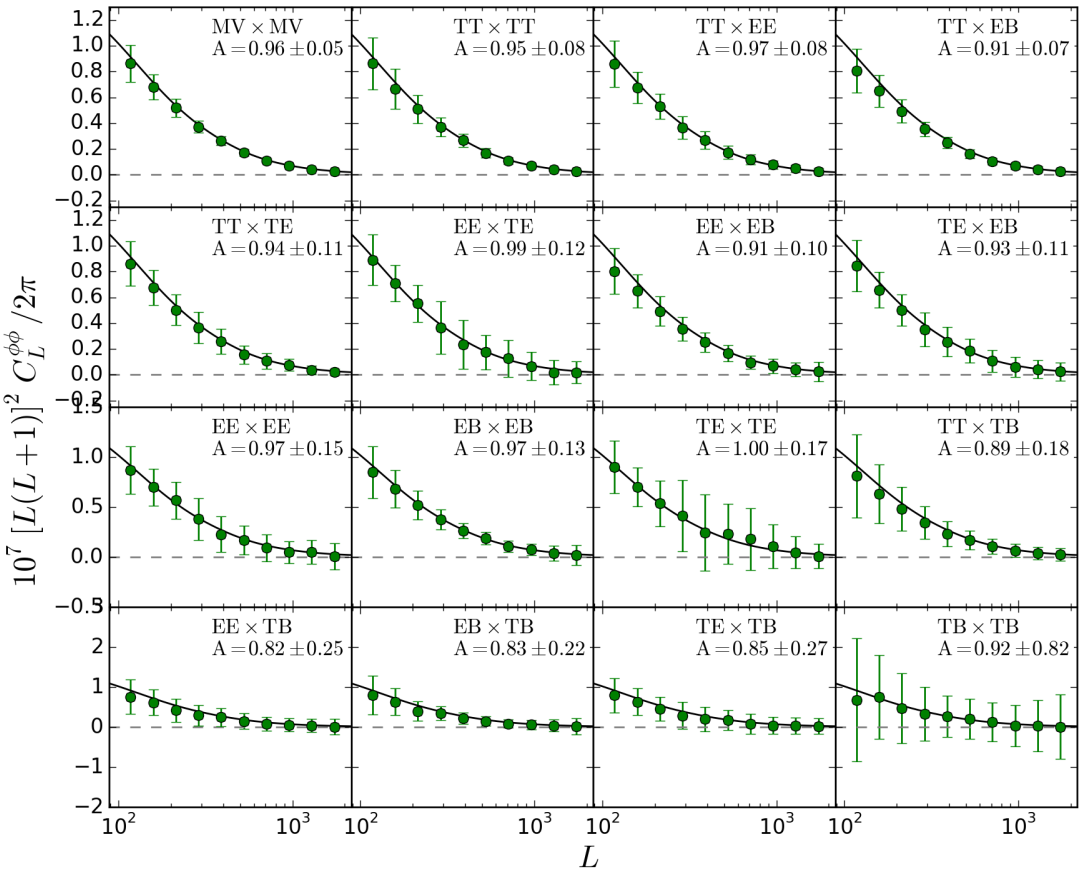

Figure 5.5: Lensing power spectrum for 16 estimators, averaged over 400 simulations. The theoretical curve is the same for all estimators, and is the input to the simulations.

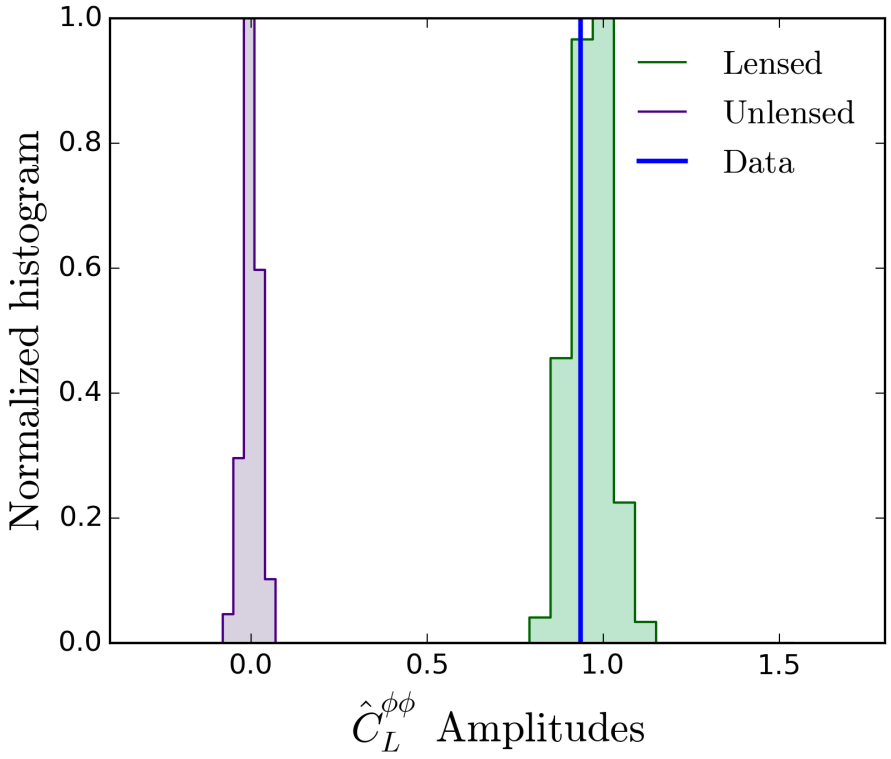

Figure 5.6: Histogram of MV lensing amplitudes reconstructed from 400 simulations for lensed (green) and unlensed (purple) simulations. The MV amplitude of the data appears as the blue vertical line. The precision of the data amplitude measurement can be quantified from the variance in the lensed simulations, while the significance of the rejection of the no-lensing hypothesis can be computed by comparing the data amplitude to the variance in the unlensed simulations.

CHAPTER 6

RESULTS

In this chapter, we present the main results of this analysis: the reconstructed lensing potential, its power spectrum, and the amplitude of the spectrum relative to the *Planck* best-fit model.

6.1 Lensing potential

The reconstructed MV κ map is shown in Figure 6.1. The κ map (defined in Equation 4.5) is a representation of the fractional overdensity of matter projected along the line of sight, with positive values showing overdensities that magnify the CMB, and negative values showing underdensities that demagnify it. κ is also a representation of $\frac{1}{2}L(L+1)\hat{\phi}_{\mathbf{L}}$ in real space, with $\hat{\phi}_{\mathbf{L}}$ from Equation 4.15.

This is a high signal to noise map. Figure 6.2 compares the reconstruction noise levels for the κ map to the theoretical lensing spectrum, showing that we measure modes between $100 < L < 220$ with a signal-to-noise ratio above unity. This map has the highest signal-to-noise per mode of reconstructions performed from the CMB so far.

This lensing reconstruction can be used in conjunction with the E-modes measured by SPTpol to delens the BICEP2/*Keck Array* B-modes, since they are observing the same patch of sky. It can also be used for cross-correlation with other tracers of large scale structure, such as optical DES data, whose footprint covers this patch of sky.

Figure 6.3 also shows maps from the five individual estimators next to the MV map.

6.2 Power spectrum of the lensing potential

We present results for the power spectrum of the lensing potential ϕ. We compute band-powers in 10 logarithmically spaced bins between $100 < L < 2000$. We compute the power

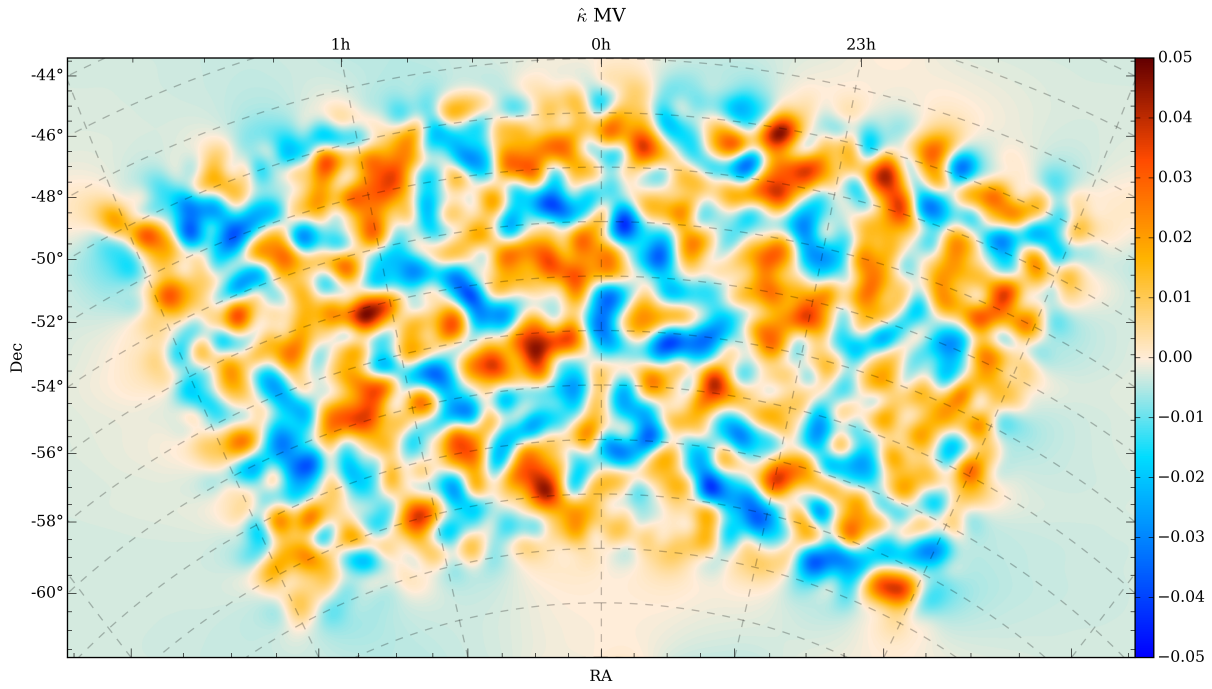

Figure 6.1: The reconstructed MV lensing potential κ map. This is a representation of the fractional overdensity of matter integrated along the line of sight, constructed from all of the available temperature and polarization data. The map has been smoothed with a 1 degree Gaussian.

spectra for all pairs of individual estimators, and then combine all estimators into a MV estimate, and all the polarization estimates into a POL estimator. The power spectra of the MV and POL ϕ estimators are shown in Figure 6.4. The MV bandpowers are listed in Table 6.1.

We find an amplitude of $A_{\rm MV} = 0.94 \pm 0.05\,({\rm stat.}) \pm 0.04\,({\rm sys.})$ for the minimum variance spectrum and $A_{\rm POL} = 0.99 \pm 0.09\,({\rm stat.}) \pm 0.05\,({\rm sys.})$ for the polarization-only spectrum. This translates to measuring the MV amplitude with a precision of 6%, equivalent to a 17.1σ constraint. The precision becomes 11% if we include systematic errors. For the POL estimator, the precision is 9%, equivalent to a 11.1σ constraint, or 15% including systematic errors. The systematic error budget is described in Chapter 7.

We calculate the χ^2 of the data amplitude relative to the fiducial *Planck* best-fit theory

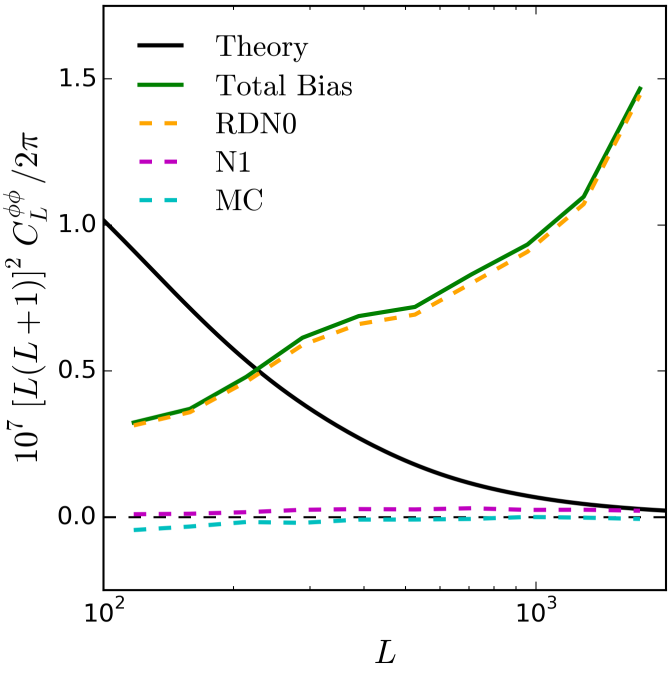

Figure 6.2: Reconstruction noise levels for the lensing potential. The black solid line is the theoretical best-fit *Planck* lensing spectrum. The realization-dependent N0 (RDN0) bias term is shown in dashed yellow. The N1 bias is shown in dashed purple. The total bias is the sum of these two terms and is shown as the solid green line. This total bias shows the reconstruction noise level. This figure shows that the reconstructed potential is measured with a signal-to-noise ratio greater than 1 for $100 < L \lesssim 220$. The MC bias is shown in dashed cyan.

spectrum used throughout this work and compare it to the χ^2 values for all of the simulation spectra. We find a probability to exceed (PTE) of 0.92 for the MV amplitude, and 0.71 for POL, so our data is in good agreement with the model.

We calculate the significance of our rejection of the no-lensing hypothesis by comparing the measured amplitude of the data to the variance in the unlensed simulations, as shown in Figure 5.6. This results in a 41σ rejection for the MV estimator and a 19.8σ for the POL estimator.

Our rejection of the no-lensing hypothesis has a higher significance value than the con-

$[L_{\rm min}$	$L_{\rm max}]$	L_b	$10^7[L_b(L_b+1)]^2\hat{C}_b^{\phi\phi}/2\pi$
[100	133]	117	0.709 ± 0.142
[134	181]	158	0.617 ± 0.097
[182	244]	213	0.514 ± 0.069
[245	330]	288	0.355 ± 0.047
[331	446]	389	0.248 ± 0.033
[447	602]	525	0.177 ± 0.024
[603	813]	708	0.113 ± 0.018
[814	1097]	956	0.063 ± 0.013
[1098	1481]	1290	0.043 ± 0.010
[1482	1998]	1741	0.034 ± 0.010

Table 6.1: Bandpowers.

straint we place on the lensing amplitude (see Figure 5.6). This is because we are dominated by the sample variance of the lenses for modes below $L \sim 220$, which can be reduced by observing a larger sky area. However, we strongly detect the effects of lensing.

Figure 6.5 shows this lensing power spectrum measurement alongside other recent measurements. The *Planck* team [5] measured the lensing spectrum with a higher precision, 2.5% (40σ), as the lensing map covers ∼70% of the sky, but the noise levels are higher such that the signal-to-noise per mode is unity only for a few modes around $L \sim 50$. The ACTpol team [7] placed a 14% constraint on the lensing amplitude (7.1σ). The POLARBEAR team [8] detected lensing at 4.2σ in polarization alone.

The *Planck* team find a mild tension between their four-point $C_\ell^{\phi\phi}$ measurement and the prediction from the best-fitting ΛCDM model [22], with the two-point function preferring higher lensing with $A_L = 1.22 \pm 0.10$ (*Planck* TT+lowP). Our data appear consistent with the *Planck* four-point function and will add another data point in context of this mild tension.

The power spectra between pairs of individual estimators are shown in Figure 6.6. They are consistent within error bars.

The next step is to run CosmoMC chains using the lensing spectrum and its covariance as inputs, and derive cosmological parameter constraints from this measurement. The 5% constraint we place on the MV lensing amplitude is comparable to the *Planck* temperature-

only constraint of 4% [35], and so we expect to be able to produce interesting cosmological constraints.

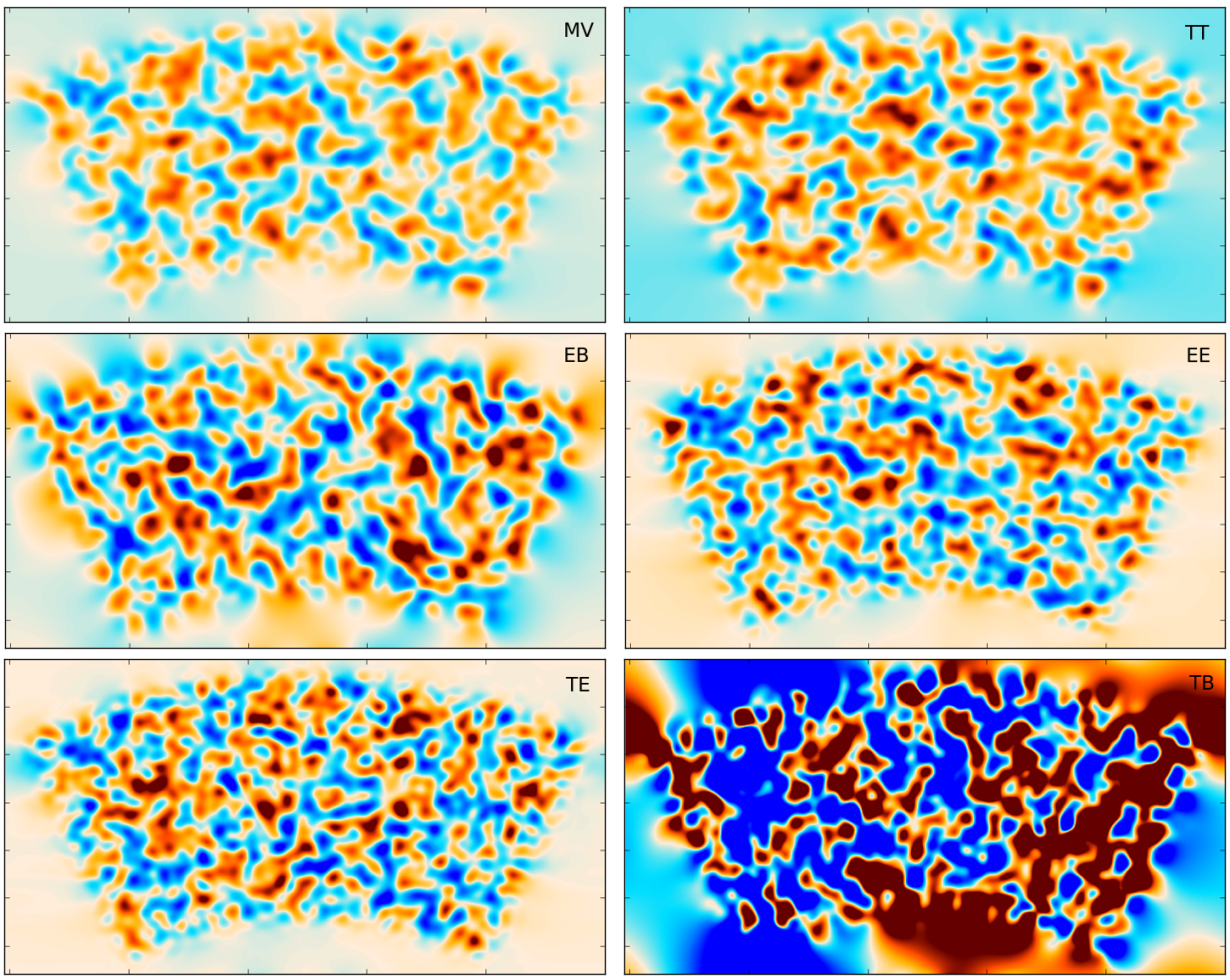

Figure 6.3: The reconstructed lensing map for the MV estimator and for the five individual estimators: TT, EE, TE, EB, and TB, plotted on the same color scale as Figure 6.1. The estimators are plotted in decreasing order of their signal-to-noise ratio. The similarity between them is visible.

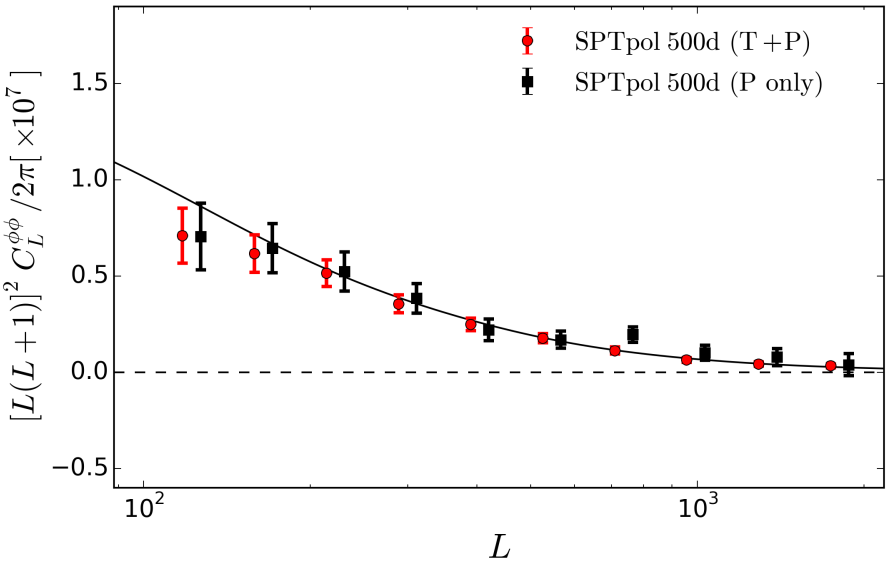

Figure 6.4: Power spectrum of the lensing potential for MV and POL estimators. The solid line shows the best-fit power spectrum from *Planck*.

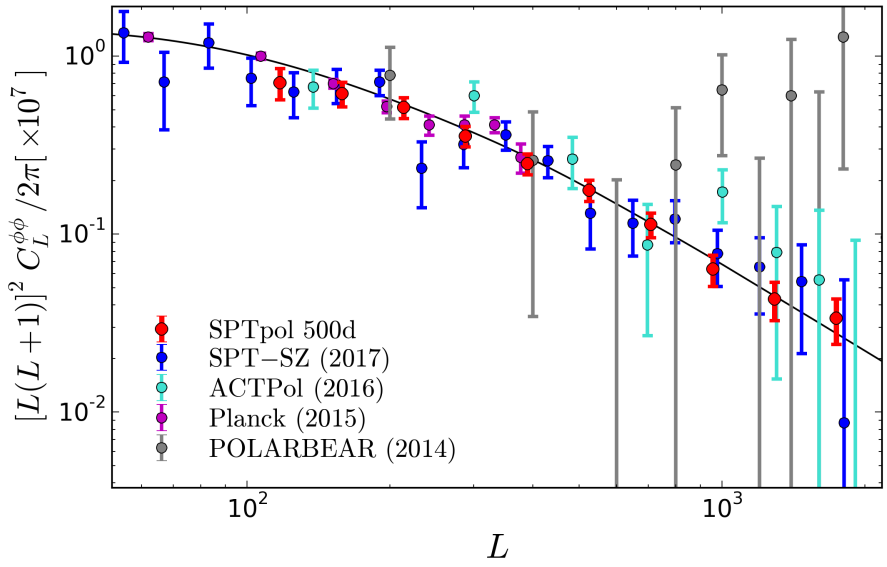

Figure 6.5: Power spectrum of the lensing potential from this analysis, plotted alongside recent measurements from *Planck* [5], SPT-SZ [6], ACTPol [7], and POLARBEAR [8].

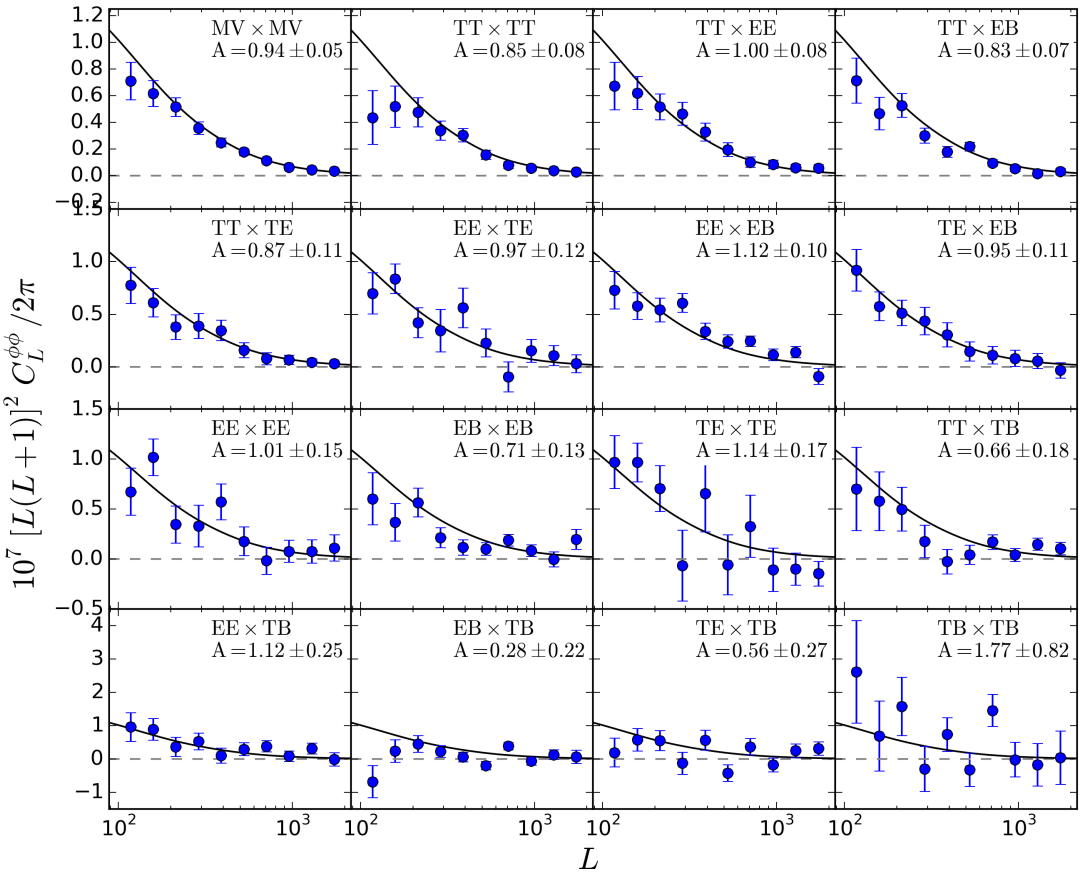

Figure 6.6: Power spectrum of the lensing potential for 15 pairs of estimators, shown next to the MV combination. The amplitudes relative to the *Planck* fit are printed for each case.

CHAPTER 7

UNCERTAINTY BUDGET AND SYSTEMATIC TESTS

Uncertainties on the lensing spectrum consist of sample and noise variance, calibration and beam errors. In Chapter 5, we used 400 simulations to compute the variance due to sample and noise. This variance represents the statistical uncertainty in our measurement. We now discuss sources of systematic uncertainty below.

7.1 Sources of uncertainty

We consider the following sources of systematic uncertainty in the lensing amplitude measurement:

1. Calibration. The absolute calibration uncertainty from the cross-correlation between the SPTpol and *Planck* map over the survey field is 0.3%. The beam measurement errors are under 1.5% over the whole ℓ range that we use, and under 0.3% for $\ell > 800$ (from Henning et al., in prep), but we use a conservative overall 1.5% term. We get $\delta_{T_{\rm cal}} = 1.8\%$, which we propagate into the lensing amplitude uncertainty as $\Delta A_{T_{\rm cal}} = A[(1+\delta_{T_{\rm cal}})^4 - 1] = 0.017$.

2. Polarization calibration. The polarization calibration uncertainty, calculated from the ratio of an EE cross-spectrum between *Planck* and SPTpol E-mode maps over the range $500 < \ell < 1500$, is $\delta_{P_{cal}} = 1\%$. We propagate this into the lensing amplitude uncertainty for the POL estimator as $\Delta A^{\rm POL}_{P_{\rm cal}} = A[(1+\delta_{P_{\rm cal}})^4 - 1] = 0.025$. We then obtain the uncertainty on the MV amplitude by computing the change in the analytic normalization $\mathcal{R}^{POL,\rm Analytic}_{\mathbf{L}}$ when we shift P_{cal} by $\delta_{P_{cal}} = 1\%$, which yields $\Delta A^{\rm MV}_{P_{\rm cal}} = 0.012$.

3. Foregrounds. We consider the effects of extragalactic and galactic foregrounds on our lensing measurement, in temperature and polarization data.

(a) Gaussian. Gaussian foreground power is picked up by the RDN0 bias calculation (which combines data and simulations) described in Section 4.3.1 and is subtracted from the lensing spectrum.

Temperature. Bright point sources are masked in the maps down to a 6.4 mJy threshold. The simulations in described in Chapter 5 contain our best estimates of residual Gaussian foreground power in temperature.

Polarization. Henning et al. (in prep) place an upper limit on polarized point source power of $D^{PS}_{\ell=3000} = 0.099\ \mu K^2$ from the E-mode power spectrum of this same 500 deg^2 SPTpol field with a point source masking threshold of 50 mJy, which is significantly higher than ours. Thus, residual polarized point source power is too low to be detected in this data, and has a negligible contribution to RDN0. Polarized galactic dust power is added to the simulations (see Chapter 5), and is also removed through RDN0.

(b) Non-Gaussian. We then look at foregrounds with a non-Gaussian signature.

Temperature. For temperature data, these were considered in [63], who looked at the effect of radio and dusty Poisson-distributed galaxies, clustered dusty galaxies, the galaxy-lensing correlation, galaxy clusters (tSZ effect), and the galaxy cluster-lensing correlation. These biases are no more than a few percent given our point source and cluster masking thresholds. We plan to subtract an estimate for these bias terms from our spectrum.

Polarization. The polarization fraction of foregrounds is estimated to be around 2% for dusty galaxies [64], and around 3.7% for radio galaxies (based on bright AGN in SPTpol data in this field). It is lower than the polarization fraction of the CMB, and so polarized non-Gaussian foregrounds will have a lower amplitude relative to the signal than in temperature, which is already small. We can thus neglect this contribution.

Type	$\Delta A_{\rm MV}$	$\Delta A_{\rm POL}$
$\Delta A_{\rm Tcal}$	0.017	0.017
$\Delta A_{\rm Pcal}$	0.012	0.025
$\Delta A_{\rm MC}$	0.036	0.038
$\Delta A_{\rm tot}$	0.04	0.05

Table 7.1: The systematic uncertainty terms. The total systematic uncertainty, $\Delta A_{\rm tot}$, is the quadrature sum of the individual uncertainties.

4. MC bias. The lensing amplitude recovered from simulations is 3.8% low for the MV estimator and 3.8% low for POL. If we do not correct for this, we can incorporate it as a $A\delta_{\rm MC}$ systematic uncertainty of $\Delta^{\rm MC}_{\rm MV} = 0.036$ and $\Delta^{\rm MC}_{\rm POL} = 0.038$. We plan to apply an additive correction to the data based on this difference, so this will be replaced by the uncertainty on that correction, which we can compute based on the difference between considering an additive versus a multiplicative correction.

All of those contributions are listed in Table 7.1. The total systematic uncertainty is the quadrature sum of the individual error terms.

7.2 Systematic tests

We perform a set of systematic tests for our results. We change various analysis settings and calculate the lensing spectrum and amplitude for each case, then compare the results to the baseline case.

We test for the following changes:

1. $\ell_{\rm xmin}$ cut. We vary the minimum $\ell_{\rm xmin}$ value that we use for the CMB data. We started out with a lower cut of 450, but we found from this test that we can go lower and thus set the baseline for $\ell_{\rm xmin} = 100$. We move $\ell_{\rm xmin}$ down to 50 and up to 200 and 300. The $\ell_{\rm xmin} = 50$ test passes, but we do not gain significantly in signal as we filter out modes below 100 heavily in our timestream filtering. The higher cut tests all pass, so we keep the lower limit at 100.

2. $\ell_{\rm max}$ cut. We vary the $\ell_{\rm max}$ cut for the CMB data. We started with $\ell_{\rm max}$=3000 and found that we can move this up to a $\ell_{\rm max}$=3500 baseline. The MV test passes for both 3000 and 4000, but the temperature-only test at 4000 fails with a PTE of 0.05 in the amplitude, and the spectrum shows a rise at high L. This is consistent with the expectation that foregrounds will start contributing to the spectrum as we increase the $\ell_{\rm max}$ cut, and will do so first in temperature data, where the amplitude of the foregrounds is much greater. We thus keep to the $\ell_{\rm max}$=3500 cut.

3. Apodized mask. We rerun the analysis with a cosine-apodized mask. The baseline analysis uses a tophat sky and point source mask because the C-inverse filter has an effective apodizing effect based on map noise.

4. Curl test. We replace the gradient lensing estimator with a curl estimator and rerun the analysis with the expectation to recover a null spectrum. This tests that the reconstruction is not contaminated by foregrounds or secondary effects.

For each of the tests above, we calculate the difference $\Delta C_b^{\phi\phi}$ between the lensing spectrum $C_{b,\,\rm sys}^{\phi\phi}$ and the spectrum for the baseline choices, $C_b^{\phi\phi}$. We also calculate this difference for the overall lensing amplitude, $\Delta A_{\rm MV}$:

$$\Delta C_b^{\phi\phi} = C_{b,\,\rm sys}^{\phi\phi} - C_b^{\phi\phi} \tag{7.1}$$

$$\Delta A_{\rm MV} = A_{\rm MV,sys} - A_{\rm MV}\,. \tag{7.2}$$

We then choose a metric to assess whether the test has been passed. We compute a χ^2 for the difference spectrum based on how much the data spectrum changes relative to the variance in the simulation difference spectrum:

$$\chi^2_{\rm sys} = \sum_b \frac{(\Delta C_{b,\,\rm data}^{\phi\phi})^2}{\sigma^2_{b,\,\rm sys}}\,. \tag{7.3}$$

Test Name	$\chi^2_{\rm sys}$	(PTE)	$\Delta\ A_{\rm MV}$ $\pm$var($\Delta A_{\rm MV,sim}$)	(PTE)
$l_{\rm xmin} = 50$	10.2	(0.419)	0.00340 ± 0.01239	(0.787)
$l_{\rm xmin} = 200$	9.4	(0.499)	0.00093 ± 0.03351	(0.963)
$l_{\rm xmin} = 300$	9.5	(0.488)	0.01246 ± 0.03721	(0.775)
$l_{\rm max} = 3000$	9.5	(0.488)	0.01246 ± 0.03721	(0.775)
$l_{\rm max} = 4000$	6.7	(0.750)	-0.01096 ± 0.01560	(0.515)
Apodized Mask	15.5	(0.115)	0.02876 ± 0.01263	(0.110)
Curl	6.7	(0.749)	-0.01700 ± 0.07361	(0.860)

Table 7.2: Results of systematics tests for the MV estimator. For each test, the χ^2 and PTE of the $C_L^{\phi\phi}$ spectrum are shown in the second column. The change in amplitude and associated PTE are shown in the third column.

This evaluates the change in the data spectrum relative to the expected change from the simulations.

We also quantify the change in overall amplitude. We calculate the difference amplitude for the data and for every simulation. We take the variance of the difference among all simulations, which evaluates the expected change. We then calculate the PTE of the data difference amplitude as the fraction of simulations that exceed the difference amplitude of the data.

We show the lensing spectra for all systematic tests and the corresponding differences from the baseline in Figure 7.1. We also summarize the systematic tests results in Table 7.2.

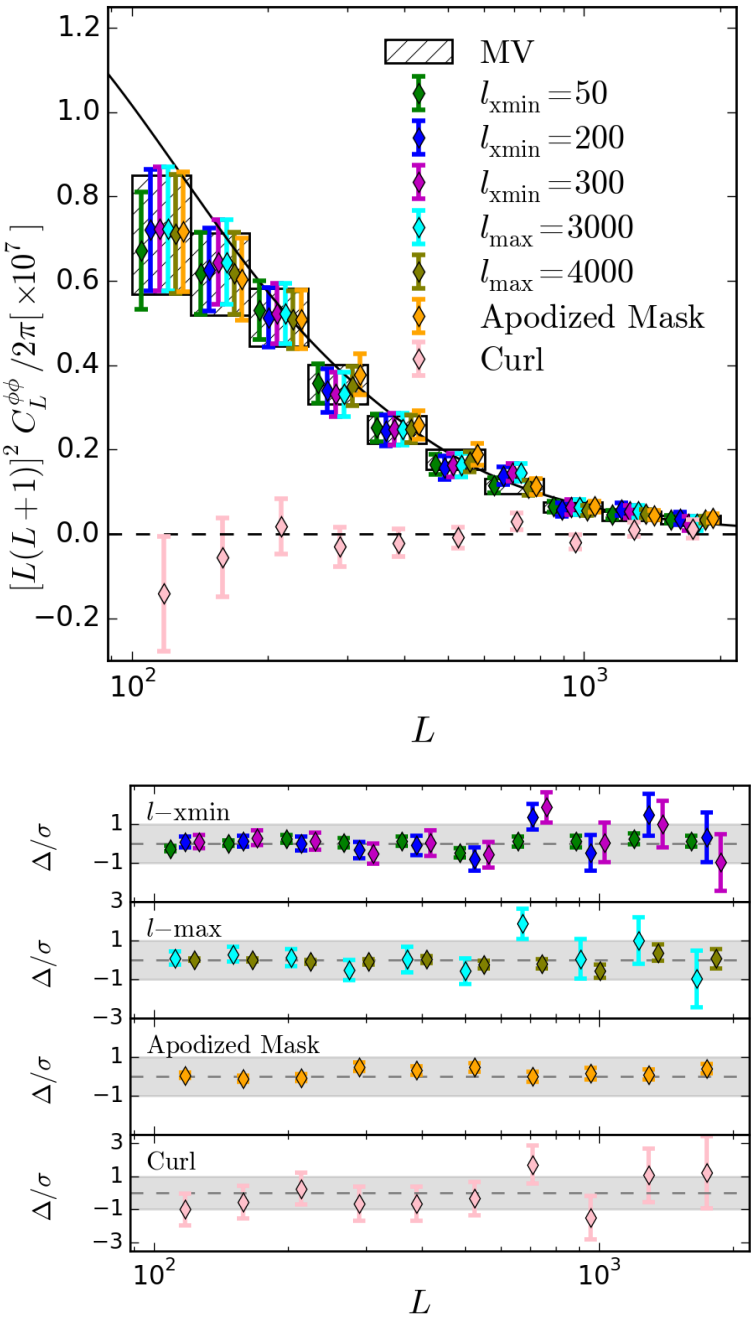

Figure 7.1: Systematic test power spectra. The top figure shows the power spectrum for each test, next to the baseline MV spectrum (hashed rectangles). The bottom figures show the same spectra plotted as $\Delta C_b^{\phi\phi}$ from 7.1 (the difference between the test and the baseline), divided by the statistical error on the baseline spectrum. The error bars are the variance expected from simulations, $\sigma_{b,\,\rm sys}$. The grey band shows the statistical error on the MV spectrum (σ) and sits at unity because we divide $\Delta C_b^{\phi\phi}$ and $\sigma_{b,\,\rm sys}$ by this value.

CHAPTER 8

OUTLOOK

In this work, we have presented a high signal-to-noise reconstruction of the CMB gravitational lensing potential and a measurement of its power spectrum. We have calculated the amplitude of this power spectrum relative to a *Planck* theory spectrum to be $A_{\rm MV} = 0.94 \pm 0.05\,({\rm Stat.}) \pm 0.04\,({\rm Sys.})$, which represents a 6% (17.1σ constraint) measurement of the amplitude. We have also rejected the no-lensing hypothesis at 41σ.

Lensing measurements from the CMB will become extremely powerful in the near future. Third generation experiments like SPT-3G and AdvACT, with low instrumental noise levels, are currently taking data. With them, lensing is becoming one of the main sources of new information for cosmological constraints. Lensing will start to drive the constraints on the sum of neutrino masses and improve dark energy measurements. The Simons Array and Simons Observatory are on the horizon. Lensing measurements from the proposed future Stage 4 experiment, CMB-S4, with even lower noise and wider sky coverage, can start distinguishing between the neutrino mass hierarchies and place tight constraints on the equation of state of dark energy and the curvature of the universe.

Lensing reconstructions are currently driven by the TT estimator, and the reconstruction noise is dominated by the sample variance of the CMB anisotropies. As polarization maps get deeper with more data and improved instruments, this will start to change: the EB estimator will gain more weight with an experiment like SPT-3G, and will eventually provide the main contribution to the minimum variance reconstruction for a CMB-Stage 4 experiment. This is shown in Figure 8.1.

The EB estimator has the advantage of both lower astrophysical foregrounds, since the polarization fields are much cleaner of contamination on arcminute scales, and greatly reduced reconstruction noise due to the absence of noise variance from unlensed small-scale B-modes, which will allow low-noise mapping of the lensing potential down to smaller scales.

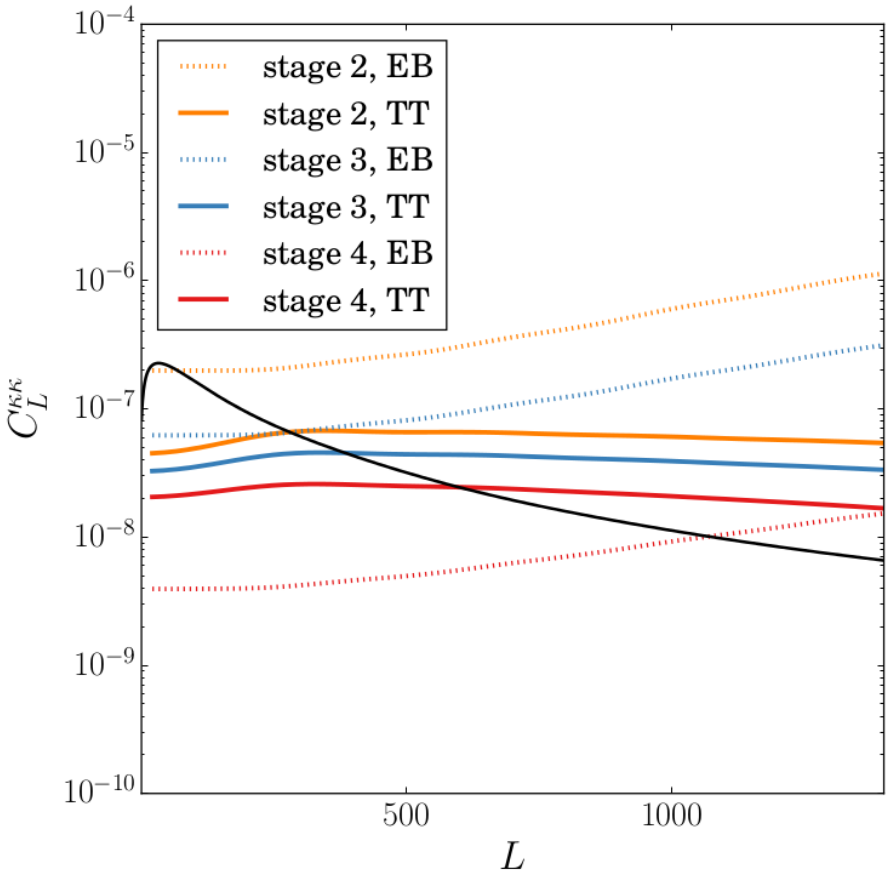

Figure 8.1: Signal and noise-per-mode levels for the lensing reconstruction for 3 experiments, similar to Figure 6.2. "Stage 2" stands for a second generation experiment like SPTpol or ACTPol. "Stage 3" is a current, third generation experiment like SPT-3G or AdvACT. "Stage 4" stands for the proposed CMB-S4. Taken from [9].

CMB-S4 is projected to be sample variance limited in the lensing potential up to $L \sim 1000$ scales [9].

With the much improved sensitivity levels in the near future, data analysis will become a greater challenge as well. Work needs to go both into handling the increased data volume and refining the analysis techniques in order to keep systematic errors low. In particular, detailed foreground bias studies will need to be performed for lensing via simulations, and improved estimator implementation will likely be required for this and, for instance, for addressing effects from nonlinear large scale structure.

Cross-correlations with datasets such as DES or future data from LSST, WFIRST and Euclid will provide tests of general relativity, probe the geometry of the universe and dark energy, improve neutrino mass constraints, measure galaxy bias and help calibrate the shear multiplicative bias [9].

Using the deep E-mode map measurements and a lensing convergence map, either reconstructed internally or using a tracer for the large scale structure such as the cosmic infrared background from dusty star-forming galaxies, one can produce a map of the lensing B-modes and use it to reduce their amplitude, in a process known as delensing.

With sensitive new experiments, accurate delensing is becoming a requirement, not only for measuring the tensor-to-scalar ratio, but also going beyond that to start constraining the shape of primordial tensor power spectrum. An iterative delensing procedure will work best for this, with successive B-mode cleaning and lensing reconstruction steps. Delensing will also improve parameter constraints; delensing the temperature and E-mode power spectra can break the degeneracy between the effective number of relativistic species $N_{\rm eff}$ and the primordial helium fraction $Y_{\rm P}$.

Future CMB lensing measurements, especially from polarization data, hold the promise to significantly advance our understanding of the universe.

REFERENCES

[1] Planck Collaboration, N. Aghanim, M. Arnaud, M. Ashdown, J. Aumont, C. Baccigalupi, A. J. Banday, R. B. Barreiro, J. G. Bartlett, N. Bartolo, and et al. Planck 2015 results. XI. CMB power spectra, likelihoods, and robustness of parameters. *Astron. Astrophys.*, 594:A11, September 2016. doi: 10.1051/0004-6361/201526926.

[2] T. Namikawa. Cosmology from weak lensing of CMB. *Progress of Theoretical and Experimental Physics*, 2014(6):06B108, June 2014. doi: 10.1093/ptep/ptu044.

[3] K. N. Abazajian, K. Arnold, J. Austermann, B. A. Benson, C. Bischoff, J. Bock, J. R. Bond, J. Borrill, I. Buder, D. L. Burke, E. Calabrese, J. E. Carlstrom, C. S. Carvalho, C. L. Chang, H. C. Chiang, S. Church, A. Cooray, T. M. Crawford, B. P. Crill, K. S. Dawson, S. Das, M. J. Devlin, M. Dobbs, S. Dodelson, O. Doré, J. Dunkley, J. L. Feng, A. Fraisse, J. Gallicchio, S. B. Giddings, D. Green, N. W. Halverson, S. Hanany, D. Hanson, S. R. Hildebrandt, A. Hincks, R. Hlozek, G. Holder, W. L. Holzapfel, K. Honscheid, G. Horowitz, W. Hu, J. Hubmayr, K. Irwin, M. Jackson, W. C. Jones, R. Kallosh, M. Kamionkowski, B. Keating, R. Keisler, W. Kinney, L. Knox, E. Komatsu, J. Kovac, C.-L. Kuo, A. Kusaka, C. Lawrence, A. T. Lee, E. Leitch, A. Linde, E. Linder, P. Lubin, J. Maldacena, E. Martinec, J. McMahon, A. Miller, V. Mukhanov, L. Newburgh, M. D. Niemack, H. Nguyen, H. T. Nguyen, L. Page, C. Pryke, C. L. Reichardt, J. E. Ruhl, N. Sehgal, U. Seljak, L. Senatore, J. Sievers, E. Silverstein, A. Slosar, K. M. Smith, D. Spergel, S. T. Staggs, A. Stark, R. Stompor, A. G. Vieregg, G. Wang, S. Watson, E. J. Wollack, W. L. K. Wu, K. W. Yoon, O. Zahn, and M. Zaldarriaga. Inflation physics from the cosmic microwave background and large scale structure. *Astroparticle Physics*, 63:55–65, March 2015. doi: 10.1016/j.astropartphys.2014.05.013.

[4] A. Lewis and A. Challinor. Weak gravitational lensing of the CMB. *Phys. Rep.*, 429: 1–65, June 2006. doi: 10.1016/j.physrep.2006.03.002.

[5] Planck Collaboration, P. A. R. Ade, N. Aghanim, M. Arnaud, M. Ashdown, J. Aumont, C. Baccigalupi, A. J. Banday, R. B. Barreiro, J. G. Bartlett, and et al. Planck 2015 results. XV. Gravitational lensing. *Astron. Astrophys.*, 594:A15, September 2016. doi: 10.1051/0004-6361/201525941.

[6] Y. Omori, R. Chown, G. Simard, K. T. Story, K. Aylor, E. J. Baxter, B. A. Benson, L. E. Bleem, J. E. Carlstrom, C. L. Chang, H. Cho, T. M. Crawford, A. T. Crites, T. de Haan, M. A. Dobbs, W. B. Everett, E. M. George, N. W. Halverson, N. L. Harrington, G. P. Holder, Z. Hou, W. L. Holzapfel, J. D. Hrubes, L. Knox, A. T. Lee, E. M. Leitch, D. Luong-Van, A. Manzotti, D. P. Marrone, J. J. McMahon, S. S. Meyer, L. M. Mocanu, J. J. Mohr, T. Natoli, S. Padin, C. Pryke, C. L. Reichardt, J. E. Ruhl, J. T. Sayre, K. K. Schaffer, E. Shirokoff, Z. Staniszewski, A. A. Stark, K. Vanderlinde, J. D. Vieira, R. Williamson, and O. Zahn. A 2500 square-degree CMB lensing map from combined South Pole Telescope and Planck data. *ArXiv e-prints*, May 2017.

[7] B. D. Sherwin, A. van Engelen, N. Sehgal, M. Madhavacheril, G. E. Addison, S. Aiola, R. Allison, N. Battaglia, J. A. Beall, D. T. Becker, J. R. Bond, E. Calabrese, R. Datta, M. J. Devlin, R. Dunner, J. Dunkley, A. E. Fox, P. Gallardo, M. Halpern, M. Hasselfield, S. Henderson, J. C. Hill, G. C. Hilton, J. Hubmayr, J. P. Hughes, A. D. Hincks, R. Hlozek, K. M. Huffenberger, B. Koopman, A. Kosowsky, T. Louis, L. Maurin, J. McMahon, K. Moodley, S. Naess, F. Nati, L. Newburgh, M. D. Niemack, L. A. Page, J. Sievers, D. N. Spergel, S. T. Staggs, R. J. Thornton, J. Van Lanen, E. Vavagiakis, and E. J. Wollack. The Atacama Cosmology Telescope: Two-Season ACTPol Lensing Power Spectrum. *ArXiv e-prints*, November 2016.

[8] The Polarbear Collaboration: P. A. R. Ade, Y. Akiba, A. E. Anthony, K. Arnold, M. Atlas, D. Barron, D. Boettger, J. Borrill, S. Chapman, Y. Chinone, M. Dobbs, T. Elleflot, J. Errard, G. Fabbian, C. Feng, D. Flanigan, A. Gilbert, W. Grainger, N. W. Halverson, M. Hasegawa, K. Hattori, M. Hazumi, W. L. Holzapfel, Y. Hori, J. Howard, P. Hyland, Y. Inoue, G. C. Jaehnig, A. H. Jaffe, B. Keating, Z. Kermish, R. Keskitalo, T. Kisner, M. Le Jeune, A. T. Lee, E. M. Leitch, E. Linder, M. Lungu, F. Matsuda, T. Matsumura, X. Meng, N. J. Miller, H. Morii, S. Moyerman, M. J. Myers, M. Navaroli, H. Nishino, A. Orlando, H. Paar, J. Peloton, D. Poletti, E. Quealy, G. Rebeiz, C. L. Reichardt, P. L. Richards, C. Ross, I. Schanning, D. E. Schenck, B. D. Sherwin, A. Shimizu, C. Shimmin, M. Shimon, P. Siritanasak, G. Smecher, H. Spieler, N. Stebor, B. Steinbach, R. Stompor, A. Suzuki, S. Takakura, T. Tomaru, B. Wilson, A. Yadav, and O. Zahn. A Measurement of the Cosmic Microwave Background B-mode Polarization Power Spectrum at Sub-degree Scales with POLARBEAR. *Ap.J.*, 794:171, October 2014. doi: 10.1088/0004-637X/794/2/171.

[9] K. N. Abazajian, P. Adshead, Z. Ahmed, S. W. Allen, D. Alonso, K. S. Arnold, C. Baccigalupi, J. G. Bartlett, N. Battaglia, B. A. Benson, C. A. Bischoff, J. Borrill, V. Buza, E. Calabrese, R. Caldwell, J. E. Carlstrom, C. L. Chang, T. M. Crawford, F.-Y. Cyr-Racine, F. De Bernardis, T. de Haan, S. di Serego Alighieri, J. Dunkley, C. Dvorkin, J. Errard, G. Fabbian, S. Feeney, S. Ferraro, J. P. Filippini, R. Flauger, G. M. Fuller, V. Gluscevic, D. Green, D. Grin, E. Grohs, J. W. Henning, J. C. Hill, R. Hlozek, G. Holder, W. Holzapfel, W. Hu, K. M. Huffenberger, R. Keskitalo, L. Knox, A. Kosowsky, J. Kovac, E. D. Kovetz, C.-L. Kuo, A. Kusaka, M. Le Jeune, A. T. Lee, M. Lilley, M. Loverde, M. S. Madhavacheril, A. Mantz, D. J. E. Marsh, J. McMahon, P. D. Meerburg, J. Meyers, A. D. Miller, J. B. Munoz, H. N. Nguyen, M. D. Niemack, M. Peloso, J. Peloton, L. Pogosian, C. Pryke, M. Raveri, C. L. Reichardt, G. Rocha, A. Rotti, E. Schaan, M. M. Schmittfull, D. Scott, N. Sehgal, S. Shandera, B. D. Sherwin, T. L. Smith, L. Sorbo, G. D. Starkman, K. T. Story, A. van Engelen, J. D. Vieira, S. Watson, N. Whitehorn, and W. L. Kimmy Wu. CMB-S4 Science Book, First Edition. *ArXiv e-prints*, October 2016.

[10] E. Hubble. A Relation between Distance and Radial Velocity among Extra-Galactic Nebulae. *Proceedings of the National Academy of Science*, 15:168–173, March 1929. doi: 10.1073/pnas.15.3.168.

[11] A. H. Guth. Inflationary universe: A possible solution to the horizon and flatness problems. *Phys. Rev. D*, 23:347–356, January 1981. doi: 10.1103/PhysRevD.23.347.

[12] W. Hu and T. Okamoto. Mass Reconstruction with Cosmic Microwave Background Polarization. *Ap.J.*, 574:566–574, August 2002. doi: 10.1086/341110.

[13] G. F. Smoot, C. L. Bennett, A. Kogut, E. L. Wright, J. Aymon, N. W. Boggess, E. S. Cheng, G. de Amici, S. Gulkis, M. G. Hauser, G. Hinshaw, P. D. Jackson, M. Janssen, E. Kaita, T. Kelsall, P. Keegstra, C. Lineweaver, K. Loewenstein, P. Lubin, J. Mather, S. S. Meyer, S. H. Moseley, T. Murdock, L. Rokke, R. F. Silverberg, L. Tenorio, R. Weiss, and D. T. Wilkinson. Structure in the COBE differential microwave radiometer first-year maps. *Ap.J. Lett.*, 396:L1–L5, September 1992. doi: 10.1086/186504.

[14] W. Hu and M. White. A CMB polarization primer. *New Astronomy*, 2:323–344, October 1997. doi: 10.1016/S1384-1076(97)00022-5.

[15] R. A. Alpher, H. Bethe, and G. Gamow. The Origin of Chemical Elements. *Physical Review*, 73:803–804, April 1948. doi: 10.1103/PhysRev.73.803.

[16] A. A. Penzias and R. W. Wilson. A Measurement of Excess Antenna Temperature at 4080 Mc/s. *Ap.J.*, 142:419–421, July 1965. doi: 10.1086/148307.

[17] J. C. Mather, E. S. Cheng, D. A. Cottingham, R. E. Eplee, Jr., D. J. Fixsen, T. Hewagama, R. B. Isaacman, K. A. Jensen, S. S. Meyer, P. D. Noerdlinger, S. M. Read, L. P. Rosen, R. A. Shafer, E. L. Wright, C. L. Bennett, N. W. Boggess, M. G. Hauser, T. Kelsall, S. H. Moseley, Jr., R. F. Silverberg, G. F. Smoot, R. Weiss, and D. T. Wilkinson. Measurement of the cosmic microwave background spectrum by the COBE FIRAS instrument. *Ap.J.*, 420:439–444, January 1994. doi: 10.1086/173574.

[18] G. Hinshaw, D. Larson, E. Komatsu, D. N. Spergel, C. L. Bennett, J. Dunkley, M. R. Nolta, M. Halpern, R. S. Hill, N. Odegard, L. Page, K. M. Smith, J. L. Weiland, B. Gold, N. Jarosik, A. Kogut, M. Limon, S. S. Meyer, G. S. Tucker, E. Wollack, and E. L. Wright. Nine-year Wilkinson Microwave Anisotropy Probe (WMAP) Observations: Cosmological Parameter Results. *Ap.J. Suppl.*, 208:19, October 2013. doi: 10.1088/0067-0049/208/2/19.

[19] K. T. Story, C. L. Reichardt, Z. Hou, R. Keisler, K. A. Aird, B. A. Benson, L. E. Bleem, J. E. Carlstrom, C. L. Chang, H.-M. Cho, T. M. Crawford, A. T. Crites, T. de Haan, M. A. Dobbs, J. Dudley, B. Follin, E. M. George, N. W. Halverson, G. P. Holder, W. L. Holzapfel, S. Hoover, J. D. Hrubes, M. Joy, L. Knox, A. T. Lee, E. M. Leitch, M. Lueker, D. Luong-Van, J. J. McMahon, J. Mehl, S. S. Meyer, M. Millea, J. J. Mohr, T. E. Montroy, S. Padin, T. Plagge, C. Pryke, J. E. Ruhl, J. T. Sayre, K. K. Schaffer, L. Shaw, E. Shirokoff, H. G. Spieler, Z. Staniszewski, A. A. Stark, A. van Engelen, K. Vanderlinde, J. D. Vieira, R. Williamson, and O. Zahn. A Measurement of the Cosmic Microwave Background Damping Tail from the 2500-Square-Degree SPT-SZ Survey. *Ap.J.*, 779:86, December 2013. doi: 10.1088/0004-637X/779/1/86.

[20] S. Das, T. Louis, M. R. Nolta, G. E. Addison, E. S. Battistelli, J. R. Bond, E. Calabrese, D. Crichton, M. J. Devlin, S. Dicker, J. Dunkley, R. Dünner, J. W. Fowler, M. Gralla, A. Hajian, M. Halpern, M. Hasselfield, M. Hilton, A. D. Hincks, R. Hlozek, K. M. Huffenberger, J. P. Hughes, K. D. Irwin, A. Kosowsky, R. H. Lupton, T. A. Marriage, D. Marsden, F. Menanteau, K. Moodley, M. D. Niemack, L. A. Page, B. Partridge, E. D. Reese, B. L. Schmitt, N. Sehgal, B. D. Sherwin, J. L. Sievers, D. N. Spergel, S. T. Staggs, D. S. Swetz, E. R. Switzer, R. Thornton, H. Trac, and E. Wollack. The Atacama Cosmology Telescope: temperature and gravitational lensing power spectrum measurements from three seasons of data. *J. Cosmology Astropart. Phys.*, 4:014, April 2014. doi: 10.1088/1475-7516/2014/04/014.

[21] E. M. George, C. L. Reichardt, K. A. Aird, B. A. Benson, L. E. Bleem, J. E. Carlstrom, C. L. Chang, H.-M. Cho, T. M. Crawford, A. T. Crites, T. de Haan, M. A. Dobbs, J. Dudley, N. W. Halverson, N. L. Harrington, G. P. Holder, W. L. Holzapfel, Z. Hou, J. D. Hrubes, R. Keisler, L. Knox, A. T. Lee, E. M. Leitch, M. Lueker, D. Luong-Van, J. J. McMahon, J. Mehl, S. S. Meyer, M. Millea, L. M. Mocanu, J. J. Mohr, T. E. Montroy, S. Padin, T. Plagge, C. Pryke, J. E. Ruhl, K. K. Schaffer, L. Shaw, E. Shirokoff, H. G. Spieler, Z. Staniszewski, A. A. Stark, K. T. Story, A. van Engelen, K. Vanderlinde, J. D. Vieira, R. Williamson, and O. Zahn. A Measurement of Secondary Cosmic Microwave Background Anisotropies from the 2500 Square-degree SPT-SZ Survey. *Ap.J.*, 799:177, February 2015. doi: 10.1088/0004-637X/799/2/177.

[22] Planck Collaboration, P. A. R. Ade, N. Aghanim, M. Arnaud, M. Ashdown, J. Aumont, C. Baccigalupi, A. J. Banday, R. B. Barreiro, J. G. Bartlett, and et al. Planck 2015 results. XIII. Cosmological parameters. *Astron. Astrophys.*, 594:A13, September 2016. doi: 10.1051/0004-6361/201525830.

[23] A. T. Crites, J. W. Henning, P. A. R. Ade, K. A. Aird, J. E. Austermann, J. A. Beall, A. N. Bender, B. A. Benson, L. E. Bleem, J. E. Carlstrom, C. L. Chang, H. C. Chiang, H.-M. Cho, R. Citron, T. M. Crawford, T. de Haan, M. A. Dobbs, W. Everett, J. Gallicchio, J. Gao, E. M. George, A. Gilbert, N. W. Halverson, D. Hanson, N. Harrington, G. C. Hilton, G. P. Holder, W. L. Holzapfel, S. Hoover, Z. Hou, J. D. Hrubes, N. Huang, J. Hubmayr, K. D. Irwin, R. Keisler, L. Knox, A. T. Lee, E. M. Leitch, D. Li, C. Liang, D. Luong-Van, J. J. McMahon, J. Mehl, S. S. Meyer, L. Mocanu, T. E. Montroy, T. Natoli, J. P. Nibarger, V. Novosad, S. Padin, C. Pryke, C. L. Reichardt, J. E. Ruhl, B. R. Saliwanchik, J. T. Sayre, K. K. Schaffer, G. Smecher, A. A. Stark, K. T. Story, C. Tucker, K. Vanderlinde, J. D. Vieira, G. Wang, N. Whitehorn, V. Yefremenko, and O. Zahn. Measurements of E-Mode Polarization and Temperature-E-Mode Correlation in the Cosmic Microwave Background from 100 Square Degrees of SPTpol Data. *Ap.J.*, 805:36, May 2015. doi: 10.1088/0004-637X/805/1/36.

[24] BICEP2/Keck and Planck Collaborations, P. A. R. Ade, N. Aghanim, Z. Ahmed, R. W. Aikin, K. D. Alexander, M. Arnaud, J. Aumont, C. Baccigalupi, A. J. Banday, and et al. Joint Analysis of BICEP2/Keck Array and Planck Data. *Phys. Rev. Lett.*, 114 (10):101301, March 2015. doi: 10.1103/PhysRevLett.114.101301.

[25] U. Seljak and M. Zaldarriaga. Signature of Gravity Waves in the Polarization of the Microwave Background. *Physical Review Letters*, 78:2054–2057, March 1997. doi: 10.1103/PhysRevLett.78.2054.

[26] M. Kamionkowski, A. Kosowsky, and A. Stebbins. A Probe of Primordial Gravity Waves and Vorticity. *Physical Review Letters*, 78:2058–2061, March 1997. doi: 10.1103/PhysRevLett.78.2058.

[27] U. Seljak. Gravitational Lensing Effect on Cosmic Microwave Background Anisotropies: A Power Spectrum Approach. *Ap.J.*, 463:1, May 1996. doi: 10.1086/177218.

[28] D. Hanson, A. Challinor, and A. Lewis. Weak lensing of the CMB. *General Relativity and Gravitation*, 42:2197–2218, September 2010. doi: 10.1007/s10714-010-1036-y.

[29] M. Zaldarriaga and U. Seljak. Gravitational lensing effect on cosmic microwave background polarization. *Phys. Rev. D*, 58(2):023003, July 1998. doi: 10.1103/PhysRevD.58.023003.

[30] T. Giannantonio, P. Fosalba, R. Cawthon, Y. Omori, M. Crocce, F. Elsner, B. Leistedt, S. Dodelson, A. Benoit-Lévy, E. Gaztañaga, G. Holder, H. V. Peiris, W. J. Percival, D. Kirk, A. H. Bauer, B. A. Benson, G. M. Bernstein, J. Carretero, T. M. Crawford, R. Crittenden, D. Huterer, B. Jain, E. Krause, C. L. Reichardt, A. J. Ross, G. Simard, B. Soergel, A. Stark, K. T. Story, J. D. Vieira, J. Weller, T. Abbott, F. B. Abdalla, S. Allam, R. Armstrong, M. Banerji, R. A. Bernstein, E. Bertin, D. Brooks, E. Buckley-Geer, D. L. Burke, D. Capozzi, J. E. Carlstrom, A. Carnero Rosell, M. Carrasco Kind, F. J. Castander, C. L. Chang, C. E. Cunha, L. N. da Costa, C. B. D'Andrea, D. L. DePoy, S. Desai, H. T. Diehl, J. P. Dietrich, P. Doel, T. F. Eifler, A. E. Evrard, A. F. Neto, E. Fernandez, D. A. Finley, B. Flaugher, J. Frieman, D. Gerdes, D. Gruen, R. A. Gruendl, G. Gutierrez, W. L. Holzapfel, K. Honscheid, D. J. James, K. Kuehn, N. Kuropatkin, O. Lahav, T. S. Li, M. Lima, M. March, J. L. Marshall, P. Martini, P. Melchior, R. Miquel, J. J. Mohr, R. C. Nichol, B. Nord, R. Ogando, A. A. Plazas, A. K. Romer, A. Roodman, E. S. Rykoff, M. Sako, B. R. Saliwanchik, E. Sanchez, M. Schubnell, I. Sevilla-Noarbe, R. C. Smith, M. Soares-Santos, F. Sobreira, E. Suchyta, M. E. C. Swanson, G. Tarle, J. Thaler, D. Thomas, V. Vikram, A. R. Walker, R. H. Wechsler, and J. Zuntz. CMB lensing tomography with the DES Science Verification galaxies. *MNRAS*, 456:3213–3244, March 2016. doi: 10.1093/mnras/stv2678.

[31] K. M. Smith, O. Zahn, and O. Doré. Detection of gravitational lensing in the cosmic microwave background. *Phys. Rev. D*, 76(4):043510, August 2007. doi: 10.1103/PhysRevD.76.043510.

[32] R. Keisler, C. L. Reichardt, K. A. Aird, B. A. Benson, L. E. Bleem, J. E. Carlstrom, C. L. Chang, H. M. Cho, T. M. Crawford, A. T. Crites, T. de Haan, M. A. Dobbs, J. Dudley, E. M. George, N. W. Halverson, G. P. Holder, W. L. Holzapfel, S. Hoover, Z. Hou, J. D. Hrubes, M. Joy, L. Knox, A. T. Lee, E. M. Leitch, M. Lueker, D. Luong-Van, J. J. McMahon, J. Mehl, S. S. Meyer, M. Millea, J. J. Mohr, T. E. Montroy, T. Natoli,

S. Padin, T. Plagge, C. Pryke, J. E. Ruhl, K. K. Schaffer, L. Shaw, E. Shirokoff, H. G. Spieler, Z. Staniszewski, A. A. Stark, K. Story, A. van Engelen, K. Vanderlinde, J. D. Vieira, R. Williamson, and O. Zahn. A Measurement of the Damping Tail of the Cosmic Microwave Background Power Spectrum with the South Pole Telescope. *Ap.J.*, 743:28, December 2011. doi: 10.1088/0004-637X/743/1/28.

[33] Planck Collaboration, P. A. R. Ade, N. Aghanim, C. Armitage-Caplan, M. Arnaud, M. Ashdown, F. Atrio-Barandela, J. Aumont, C. Baccigalupi, A. J. Banday, and et al. Planck 2013 results. XV. CMB power spectra and likelihood. *Astron. Astrophys.*, 571: A15, November 2014. doi: 10.1051/0004-6361/201321573.

[34] A. van Engelen, R. Keisler, O. Zahn, K. A. Aird, B. A. Benson, L. E. Bleem, J. E. Carlstrom, C. L. Chang, H. M. Cho, T. M. Crawford, A. T. Crites, T. de Haan, M. A. Dobbs, J. Dudley, E. M. George, N. W. Halverson, G. P. Holder, W. L. Holzapfel, S. Hoover, Z. Hou, J. D. Hrubes, M. Joy, L. Knox, A. T. Lee, E. M. Leitch, M. Lueker, D. Luong-Van, J. J. McMahon, J. Mehl, S. S. Meyer, M. Millea, J. J. Mohr, T. E. Montroy, T. Natoli, S. Padin, T. Plagge, C. Pryke, C. L. Reichardt, J. E. Ruhl, J. T. Sayre, K. K. Schaffer, L. Shaw, E. Shirokoff, H. G. Spieler, Z. Staniszewski, A. A. Stark, K. Story, K. Vanderlinde, J. D. Vieira, and R. Williamson. A Measurement of Gravitational Lensing of the Microwave Background Using South Pole Telescope Data. *Ap.J.*, 756:142, September 2012. doi: 10.1088/0004-637X/756/2/142.

[35] Planck Collaboration, P. A. R. Ade, N. Aghanim, C. Armitage-Caplan, M. Arnaud, M. Ashdown, F. Atrio-Barandela, J. Aumont, C. Baccigalupi, A. J. Banday, and et al. Planck 2013 results. XVII. Gravitational lensing by large-scale structure. *Astron. Astrophys.*, 571:A17, November 2014. doi: 10.1051/0004-6361/201321543.

[36] D. Hanson et al. Detection of B-mode Polarization in the Cosmic Microwave Background with Data from the South Pole Telescope. *Phys.Rev.Lett.*, 111(14):141301, 2013. doi: 10.1103/PhysRevLett.111.141301.

[37] K. T. Story, D. Hanson, P. A. R. Ade, K. A. Aird, J. E. Austermann, J. A. Beall, A. N. Bender, B. A. Benson, L. E. Bleem, J. E. Carlstrom, C. L. Chang, H. C. Chiang, H.-M. Cho, R. Citron, T. M. Crawford, A. T. Crites, T. de Haan, M. A. Dobbs, W. Everett, J. Gallicchio, J. Gao, E. M. George, A. Gilbert, N. W. Halverson, N. Harrington, J. W. Henning, G. C. Hilton, G. P. Holder, W. L. Holzapfel, S. Hoover, Z. Hou, J. D. Hrubes, N. Huang, J. Hubmayr, K. D. Irwin, R. Keisler, L. Knox, A. T. Lee, E. M. Leitch, D. Li, C. Liang, D. Luong-Van, J. J. McMahon, J. Mehl, S. S. Meyer, L. Mocanu, T. E. Montroy, T. Natoli, J. P. Nibarger, V. Novosad, S. Padin, C. Pryke, C. L. Reichardt, J. E. Ruhl, B. R. Saliwanchik, J. T. Sayre, K. K. Schaffer, G. Smecher, A. A. Stark, C. Tucker, K. Vanderlinde, J. D. Vieira, G. Wang, N. Whitehorn, V. Yefremenko, and O. Zahn. A Measurement of the Cosmic Microwave Background Gravitational Lensing Potential from 100 Square Degrees of SPTpol Data. *Ap.J.*, 810:50, September 2015. doi: 10.1088/0004-637X/810/1/50.

[38] D. Kirk, Y. Omori, A. Benoit-Lévy, R. Cawthon, C. Chang, P. Larsen, A. Amara, D. Bacon, T. M. Crawford, S. Dodelson, P. Fosalba, T. Giannantonio, G. Holder, B. Jain, T. Kacprzak, O. Lahav, N. MacCrann, A. Nicola, A. Refregier, E. Sheldon, K. T. Story, M. A. Troxel, J. D. Vieira, V. Vikram, J. Zuntz, T. M. C. Abbott, F. B. Abdalla, M. R. Becker, B. A. Benson, G. M. Bernstein, R. A. Bernstein, L. E. Bleem, C. Bonnett, S. L. Bridle, D. Brooks, E. Buckley-Geer, D. L. Burke, D. Capozzi, J. E. Carlstrom, A. C. Rosell, M. C. Kind, J. Carretero, M. Crocce, C. E. Cunha, C. B. D'Andrea, L. N. da Costa, S. Desai, H. T. Diehl, J. P. Dietrich, P. Doel, T. F. Eifler, A. E. Evrard, B. Flaugher, J. Frieman, D. W. Gerdes, D. A. Goldstein, D. Gruen, R. A. Gruendl, K. Honscheid, D. J. James, M. Jarvis, S. Kent, K. Kuehn, N. Kuropatkin, M. Lima, M. March, P. Martini, P. Melchior, C. J. Miller, R. Miquel, R. C. Nichol, R. Ogando, A. A. Plazas, C. L. Reichardt, A. Roodman, E. Rozo, E. S. Rykoff, M. Sako, E. Sanchez, V. Scarpine, M. Schubnell, I. Sevilla-Noarbe, G. Simard, R. C. Smith, M. Soares-Santos, F. Sobreira, E. Suchyta, M. E. C. Swanson, G. Tarle, D. Thomas, R. H. Wechsler, and J. Weller. Cross-correlation of gravitational lensing from DES Science Verification data with SPT and Planck lensing. *MNRAS*, 459:21–34, June 2016. doi: 10.1093/mnras/stw570.

[39] E. Baxter, J. Clampitt, T. Giannantonio, S. Dodelson, B. Jain, D. Huterer, L. Bleem, T. Crawford, G. Efstathiou, P. Fosalba, D. Kirk, J. Kwan, C. Sánchez, K. Story, M. A. Troxel, T. M. C. Abbott, F. B. Abdalla, R. Armstrong, A. Benoit-Lévy, B. Benson, G. M. Bernstein, R. A. Bernstein, E. Bertin, D. Brooks, J. Carlstrom, A. C. Rosell, M. Carrasco Kind, J. Carretero, R. Chown, M. Crocce, C. E. Cunha, L. N. da Costa, S. Desai, H. T. Diehl, J. P. Dietrich, P. Doel, A. E. Evrard, A. Fausti Neto, B. Flaugher, J. Frieman, D. Gruen, R. A. Gruendl, G. Gutierrez, T. de Haan, G. Holder, K. Honscheid, Z. Hou, D. J. James, K. Kuehn, N. Kuropatkin, M. Lima, M. March, J. L. Marshall, P. Martini, P. Melchior, C. J. Miller, R. Miquel, J. J. Mohr, B. Nord, Y. Omori, A. A. Plazas, C. Reichardt, A. K. Romer, E. S. Rykoff, E. Sanchez, I. Sevilla-Noarbe, E. Sheldon, R. C. Smith, M. Soares-Santos, F. Sobreira, E. Suchyta, A. Stark, M. E. C. Swanson, G. Tarle, D. Thomas, A. R. Walker, and R. H. Wechsler. Joint measurement of lensing-galaxy correlations using SPT and DES SV data. *MNRAS*, 461:4099–4114, October 2016. doi: 10.1093/mnras/stw1584.

[40] P. Larsen, A. Challinor, B. D. Sherwin, and D. Mak. Demonstration of Cosmic Microwave Background Delensing Using the Cosmic Infrared Background. *Physical Review Letters*, 117(15):151102, October 2016. doi: 10.1103/PhysRevLett.117.151102.

[41] J. Carron, A. Lewis, and A. Challinor. Internal delensing of Planck CMB temperature and polarization. *J. Cosmology Astropart. Phys.*, 5:035, May 2017. doi: 10.1088/1475-7516/2017/05/035.

[42] A. Manzotti, K. T. Story, W. L. K. Wu, J. E. Austermann, J. A. Beall, A. N. Bender, B. A. Benson, L. E. Bleem, J. J. Bock, J. E. Carlstrom, C. L. Chang, H. C. Chiang, H. Cho, R. Citron, A. Conley, T. M. Crawford, A. T. Crites, T. de Haan, M. A. Dobbs, S. Dodelson, W. Everett, J. Gallicchio, E. M. George, A. Gilbert, N. W. Halverson,

N. Harrington, J. W. Henning, G. C. Hilton, G. P. Holder, W. L. Holzapfel, S. Hoover, Z. Hou, J. D. Hrubes, N. Huang, J. Hubmayr, K. D. Irwin, R. Keisler, L. Knox, A. T. Lee, E. M. Leitch, D. Li, J. J. McMahon, S. S. Meyer, L. M. Mocanu, T. Natoli, J. P. Nibarger, V. Novosad, S. Padin, C. Pryke, C. L. Reichardt, J. E. Ruhl, B. R. Saliwanchik, J. T. Sayre, K. K. Schaffer, G. Smecher, A. A. Stark, K. Vanderlinde, J. D. Vieira, M. P. Viero, G. Wang, N. Whitehorn, V. Yefremenko, and M. Zemcov. CMB Polarization B-mode Delensing with SPTpol and Herschel. *ArXiv e-prints*, January 2017.

[43] S. Padin, Z. Staniszewski, R. Keisler, M. Joy, A. A. Stark, P. A. R. Ade, K. A. Aird, B. A. Benson, L. E. Bleem, J. E. Carlstrom, C. L. Chang, T. M. Crawford, A. T. Crites, M. A. Dobbs, N. W. Halverson, S. Heimsath, R. E. Hills, W. L. Holzapfel, C. Lawrie, A. T. Lee, E. M. Leitch, J. Leong, W. Lu, M. Lueker, J. J. McMahon, S. S. Meyer, J. J. Mohr, T. E. Montroy, T. Plagge, C. Pryke, J. E. Ruhl, K. K. Schaffer, E. Shirokoff, H. G. Spieler, and J. D. Vieira. South pole telescope optics. *Appl. Opt.*, 47(24):4418–4428, Aug 2008. doi: 10.1364/AO.47.004418.

[44] J. E. Carlstrom, P. A. R. Ade, K. A. Aird, B. A. Benson, L. E. Bleem, S. Busetti, C. L. Chang, E. Chauvin, H.-M. Cho, T. M. Crawford, A. T. Crites, M. A. Dobbs, N. W. Halverson, S. Heimsath, W. L. Holzapfel, J. D. Hrubes, M. Joy, R. Keisler, T. M. Lanting, A. T. Lee, E. M. Leitch, J. Leong, W. Lu, M. Lueker, D. Luong-van, J. J. McMahon, J. Mehl, S. S. Meyer, J. J. Mohr, T. E. Montroy, S. Padin, T. Plagge, C. Pryke, J. E. Ruhl, K. K. Schaffer, D. Schwan, E. Shirokoff, H. G. Spieler, Z. Staniszewski, A. A. Stark, C. Tucker, K. Vanderlinde, J. D. Vieira, and R. Williamson. The 10 Meter South Pole Telescope. *PASP*, 123:568–581, May 2011. doi: 10.1086/659879.

[45] B. A. Benson, P. A. R. Ade, Z. Ahmed, S. W. Allen, K. Arnold, J. E. Austermann, A. N. Bender, L. E. Bleem, J. E. Carlstrom, C. L. Chang, H. M. Cho, J. F. Cliche, T. M. Crawford, A. Cukierman, T. de Haan, M. A. Dobbs, D. Dutcher, W. Everett, A. Gilbert, N. W. Halverson, D. Hanson, N. L. Harrington, K. Hattori, J. W. Henning, G. C. Hilton, G. P. Holder, W. L. Holzapfel, K. D. Irwin, R. Keisler, L. Knox, D. Kubik, C. L. Kuo, A. T. Lee, E. M. Leitch, D. Li, M. McDonald, S. S. Meyer, J. Montgomery, M. Myers, T. Natoli, H. Nguyen, V. Novosad, S. Padin, Z. Pan, J. Pearson, C. Reichardt, J. E. Ruhl, B. R. Saliwanchik, G. Simard, G. Smecher, J. T. Sayre, E. Shirokoff, A. A. Stark, K. Story, A. Suzuki, K. L. Thompson, C. Tucker, K. Vanderlinde, J. D. Vieira, A. Vikhlinin, G. Wang, V. Yefremenko, and K. W. Yoon. SPT-3G: a next-generation cosmic microwave background polarization experiment on the South Pole telescope. In *Millimeter, Submillimeter, and Far-Infrared Detectors and Instrumentation for Astronomy VII*, volume 9153 of *SPIE Proc.*, page 91531P, July 2014. doi: 10.1117/12.2057305.

[46] J. W. Henning, P. Ade, K. A. Aird, J. E. Austermann, J. A. Beall, D. Becker, B. A. Benson, L. E. Bleem, J. Britton, J. E. Carlstrom, C. L. Chang, H.-M. Cho, T. M. Crawford, A. T. Crites, A. Datesman, T. de Haan, M. A. Dobbs, W. Everett, A. Ewall-Wice, E. M. George, N. W. Halverson, N. Harrington, G. C. Hilton, W. L. Holzapfel, J. Hubmayr, K. D. Irwin, M. Karfunkle, R. Keisler, J. Kennedy, A. T. Lee, E. Leitch, D. Li,

M. Lueker, D. P. Marrone, J. J. McMahon, J. Mehl, S. S. Meyer, J. Montgomery, T. E. Montroy, J. Nagy, T. Natoli, J. P. Nibarger, M. D. Niemack, V. Novosad, S. Padin, C. Pryke, C. L. Reichardt, J. E. Ruhl, B. R. Saliwanchik, J. T. Sayre, K. K. Schaffer, E. Shirokoff, K. Story, C. Tucker, K. Vanderlinde, J. D. Vieira, G. Wang, R. Williamson, V. Yefremenko, K. W. Yoon, and E. Young. Feedhorn-coupled TES polarimeter camera modules at 150 GHz for CMB polarization measurements with SPTpol. In *Millimeter, Submillimeter, and Far-Infrared Detectors and Instrumentation for Astronomy VI*, volume 8452 of *Proc. SPIE*, page 84523A, September 2012. doi: 10.1117/12.927172.

[47] J. T. Sayre, P. Ade, K. A. Aird, J. E. Austermann, J. A. Beall, D. Becker, B. A. Benson, L. E. Bleem, J. Britton, J. E. Carlstrom, C. L. Chang, H.-M. Cho, T. M. Crawford, A. T. Crites, A. Datesman, T. de Haan, M. A. Dobbs, W. Everett, A. Ewall-Wice, E. M. George, N. W. Halverson, N. Harrington, J. W. Henning, G. C. Hilton, W. L. Holzapfel, J. Hubmayr, K. D. Irwin, M. Karfunkle, R. Keisler, J. Kennedy, A. T. Lee, E. Leitch, D. Li, M. Lueker, D. P. Marrone, J. J. McMahon, J. Mehl, S. S. Meyer, J. Montgomery, T. E. Montroy, J. Nagy, T. Natoli, J. P. Nibarger, M. D. Niemack, V. Novosad, S. Padin, C. Pryke, C. L. Reichardt, J. E. Ruhl, B. R. Saliwanchik, K. K. Schaffer, E. Shirokoff, K. Story, C. Tucker, K. Vanderlinde, J. D. Vieira, G. Wang, R. Williamson, V. Yefremenko, K. W. Yoon, and E. Young. Design and characterization of 90 GHz feedhorn-coupled TES polarimeter pixels in the SPTPol camera,.

[48] M. A. Dobbs, M. Lueker, K. A. Aird, A. N. Bender, B. A. Benson, L. E. Bleem, J. E. Carlstrom, C. L. Chang, H.-M. Cho, J. Clarke, T. M. Crawford, A. T. Crites, D. I. Flanigan, T. de Haan, E. M. George, N. W. Halverson, W. L. Holzapfel, J. D. Hrubes, B. R. Johnson, J. Joseph, R. Keisler, J. Kennedy, Z. Kermish, T. M. Lanting, A. T. Lee, E. M. Leitch, D. Luong-Van, J. J. McMahon, J. Mehl, S. S. Meyer, T. E. Montroy, S. Padin, T. Plagge, C. Pryke, P. L. Richards, J. E. Ruhl, K. K. Schaffer, D. Schwan, E. Shirokoff, H. G. Spieler, Z. Staniszewski, A. A. Stark, K. Vanderlinde, J. D. Vieira, C. Vu, B. Westbrook, and R. Williamson. Frequency multiplexed superconducting quantum interference device readout of large bolometer arrays for cosmic microwave background measurements. *Review of Scientific Instruments*, 83(7):073113–073113, July 2012. doi: 10.1063/1.4737629.

[49] Tijmen de Haan, Graeme Smecher, and Matt Dobbs. Improved performance of TES bolometers using digital feedback, 2012.

[50] R. Keisler, S. Hoover, N. Harrington, J. W. Henning, P. A. R. Ade, K. A. Aird, J. E. Austermann, J. A. Beall, A. N. Bender, B. A. Benson, L. E. Bleem, J. E. Carlstrom, C. L. Chang, H. C. Chiang, H.-M. Cho, R. Citron, T. M. Crawford, A. T. Crites, T. de Haan, M. A. Dobbs, W. Everett, J. Gallicchio, J. Gao, E. M. George, A. Gilbert, N. W. Halverson, D. Hanson, G. C. Hilton, G. P. Holder, W. L. Holzapfel, Z. Hou, J. D. Hrubes, N. Huang, J. Hubmayr, K. D. Irwin, L. Knox, A. T. Lee, E. M. Leitch, D. Li, D. Luong-Van, D. P. Marrone, J. J. McMahon, J. Mehl, S. S. Meyer, L. Mocanu, T. Natoli, J. P. Nibarger, V. Novosad, S. Padin, C. Pryke, C. L. Reichardt, J. E. Ruhl, B. R. Saliwanchik, J. T. Sayre, K. K. Schaffer, E. Shirokoff, G. Smecher, A. A.

Stark, K. T. Story, C. Tucker, K. Vanderlinde, J. D. Vieira, G. Wang, N. Whitehorn, V. Yefremenko, and O. Zahn. Measurements of Sub-degree B-mode Polarization in the Cosmic Microwave Background from 100 Square Degrees of SPTpol Data. *Ap.J.*, 807: 151, July 2015. doi: 10.1088/0004-637X/807/2/151.

[51] F. Couchot, J. Delabrouille, J. Kaplan, and B. Revenu. Optimised polarimeter configurations for measuring the Stokes parameters of the cosmic microwave background radiation. *Astron. Astrophys.*, 135:579–584, March 1999. doi: 10.1051/aas:1999191.

[52] W. C. Jones, T. E. Montroy, B. P. Crill, C. R. Contaldi, T. S. Kisner, A. E. Lange, C. J. MacTavish, C. B. Netterfield, and J. E. Ruhl. Instrumental and analytic methods for bolometric polarimetry. *Astron. Astrophys.*, 470:771–785, August 2007. doi: 10.1051/0004-6361:20065911.

[53] M. Zaldarriaga. Nature of the E-B decomposition of CMB polarization. *Phys. Rev. D*, 64(10):103001, November 2001. doi: 10.1103/PhysRevD.64.103001.

[54] K. M. Smith and M. Zaldarriaga. General solution to the E-B mixing problem. *Phys. Rev. D*, 76(4):043001, August 2007. doi: 10.1103/PhysRevD.76.043001.

[55] A. Blanchard and J. Schneider. Gravitational lensing effect on the fluctuations of the cosmic background radiation. *Astron. Astrophys.*, 184:1–6, October 1987.

[56] F. Bernardeau. Weak lensing detection in CMB maps. *Astron. Astrophys.*, 324:15–26, August 1997.

[57] E. F. Bunn, K. B. Fisher, Y. Hoffman, O. Lahav, J. Silk, and S. Zaroubi. Wiener filtering of the COBE Differential Microwave Radiometer data. *Ap.J. Lett.*, 432:L75–L78, September 1994. doi: 10.1086/187515.

[58] T. Namikawa, D. Hanson, and R. Takahashi. Bias-hardened CMB lensing. *MNRAS*, 431:609–620, May 2013. doi: 10.1093/mnras/stt195.

[59] M. Kesden, A. Cooray, and M. Kamionkowski. Lensing reconstruction with CMB temperature and polarization. *Phys. Rev. D*, 67(12):123507–+, June 2003. doi: 10.1103/PhysRevD.67.123507.

[60] K. M. Górski, E. Hivon, A. J. Banday, B. D. Wandelt, F. K. Hansen, M. Reinecke, and M. Bartelmann. HEALPix: A Framework for High-Resolution Discretization and Fast Analysis of Data Distributed on the Sphere. *Ap.J.*, 622:759–771, April 2005. doi: 10.1086/427976.

[61] A. Lewis. Lensed CMB simulation and parameter estimation. *Phys. Rev. D*, 71(8): 083008–+, April 2005. doi: 10.1103/PhysRevD.71.083008.

[62] L. D. Shaw, D. Nagai, S. Bhattacharya, and E. T. Lau. Impact of Cluster Physics on the Sunyaev-Zel'dovich Power Spectrum. *Ap.J.*, 725:1452–1465, December 2010. doi: 10.1088/0004-637X/725/2/1452.

[63] A. van Engelen, S. Bhattacharya, N. Sehgal, G. P. Holder, O. Zahn, and D. Nagai. CMB Lensing Power Spectrum Biases from Galaxies and Clusters Using High-angular Resolution Temperature Maps. *Ap.J.*, 786:13, May 2014. doi: 10.1088/0004-637X/786/1/13.

[64] M. Seiffert, C. Borys, D. Scott, and M. Halpern. An upper limit to polarized submillimetre emission in Arp 220. *MNRAS*, 374:409–414, January 2007. doi: 10.1111/j.1365-2966.2006.11186.x.